UNIVERSITY OF OTTAWA

MASTER'S THESIS

Analysis of Plasmonic Metastructures for Engineered Nonlinear Nanophotonics

Author:

Md SAAD-BIN-ALAM

Supervisors:

Prof. Ksenia DOLGALEVA

A thesis submitted to the University of Ottawa in partial fulfillment of the requirements for the Master of Applied Science in Electrical and Computer Engineering

uOttawa

Faculté de génie
Faculty of Engineering

School of Electrical Engineering and Computer Science
University of Ottawa

Declaration of Authorship

I, Md SAAD-BIN-ALAM, declare that this thesis, titled "Analysis of Plasmonic Metastructures for Engineered Nonlinear Nanophotonics", and the work presented in it are my own. I confirm that except where specific reference is made to the work of others, the contents of this dissertation are original and have not been submitted in whole or in part for consideration for any other degree or qualification in this, or any other university. This dissertation is my own work and contains nothing which is the outcome of work done in collaboration with others, except as specified in the text and Acknowledgements.

Md Saad-Bin-Alam
January, 2019
Ottawa, Canada

UNIVERSITY OF OTTAWA

Abstract

Faculty of Engineering

School of Electrical Engineering and Computer Science

Master of Applied Science in Electrical and Computer Engineering

Analysis of Plasmonic Metastructures for Engineered Nonlinear Nanophotonics

by Md SAAD-BIN-ALAM

This Master's dissertation focuses on engineering artificial nanostructures, namely, arrays of metamolecules on a substrate (metasurfaces), with the goal to achieve the desired linear and nonlinear optical responses. Specifically, a simple analytical model capable of predicting optical nonlinearity of an individual metamolecule has been developed. The model allows one to estimate the nonlinear optical response (linear polarizability and nonlinear hyperpolarizabilities) of a metamolecule based on the knowledge of its shape, dimensions, and material. In addition, a new experimental approach to measure hyperpolarizability has also been investigated. As another research effort, a 2D plasmonic metasurface with the collective behaviour of the metamolecules known as hybrid plasmonic-Fabry-Perot cavity and surface lattice resonances was designed, fabricated and optically characterized. We experimentally discovered a novel way of coupling the microcavity resonances and the diffraction orders of the plasmonic metamolecule arrays with the low-quality plasmon resonance to generate multiple sharp resonances with the higher quality factors. Finally, we experimentally observed and demonstrated a record ultra-high-Q surface lattice resonance from a plasmonic metasurface. These novel results can be used to render highly efficient nonlinear optical responses relying on high optical field localization, and can serve as the stepping stone towards achieving practical artificial nanophotonic devices with tailored linear and nonlinear optical responses.

Acknowledgements

At the beginning, I would like to express all the praises and thanks with utmost humbleness to almighty Allah, the most Magnificent, Beneficent, and Merciful; who bestow His blessings upon me, guide me, and help me to keep patience to successfully accomplish all the challenging and time-consuming research projects in the field of artificial nanophotonics in my Master's thesis.

Simultaneously indulging in multiple cutting-edge research projects in one of the most famous and leading optics research groups in the contemporary world is undoubtedly a rare prestigious matter and very exciting for a Master's student. I am really honored that my supervisor Prof. Ksenia Dolgaleva (Canada Research Chair in Integrated Photonics) and team leader Prof. Robert W. Boyd (Canada Excellence Research Chair in Quantum and Nonlinear Photonics) selected me for such a great opportunity. I am so much grateful and thankful to both of them for keeping faith on me till the end moment. I acknowledge all the academic moral support and encouragement they kindly provided to me. I also would like to thank them very much for awarding me the CERC fellowships (Integrated Photonics, and Quantum Photonics) for different projects.

Any state-of-the-art research project requires the expertise of multiple highly experienced experts from various background. I recognize the support of all the other team members of both of my projects. I thank a lot Prof. Kosmas Tsakmakidis (former visiting scholar in our group) for conceiving the initial theoretical idea to predict hyperpolarizability of individual plasmonic metamolecule using equivalent electrical circuit model. I also express my heartiest thanks to Dr. Mikko Huttunen (former postdoc in our group) who trained me by-hand to learn linear and nonlinear optical characterization techniques and building a complicated experimental setup in the lab at both the University of Ottawa and Tampere University.

My heartfelt thanks to Dr. Orad Reshef (current Postdoc in our group) and Dr. Kashif. M. Awan (former Ph.D. alumni in our group), who almost sacrificed enjoying the time with their own families even during the weekends and beyond office hours to fabricate the series of sophisticated artificial samples for my different projects. Dr. Reshef was also my mentor to learn the operation of numerical analysis software. Though, to be frank, these are not

the main reasons for what I am actually grateful to them. Kashif and Orad are the persons who actually have taken care of me as their younger brother. Their true love for me to make me happy all the time actually made my life easier and enjoyable as an international student staying very far from parents and siblings. I will always remember my honest friendship with these people.

I acknowledge all the fruitful discussion with Prof. John Sipe (University of Toronto), Prof. Gerd Leuchs (Max-Planck Institue of Science for Light), Prof. Nader Engheta (University of Pennsylvania), and Dr. Ekaterina Poutrina (U.S. Airforce Research) during their visit in different times at the University of Ottawa. Also, I acknowledge the discussion with Prof. Martti Kauranen (Tampere University) during my visit to Finland. I would like to thank all of them for sharing their valuable thoughts with me and frank encouragements. To be honest, I was thrilled throughout all the moments I passed with these big names.

The projects related to plasmonic metasurfaces were supported by NSERC engage program, for which we jointly worked with our industrial collaborator Iridian Spectral Technologies Ltd. Besides acknowledging the support from NSERC, I would like to thank the Chief Technical Officer (CTO) Dr. Brian Sullivan and Senior Research Scientist Dr. Graham Carlow from Iridian Spectral Technologies for their continuous support and encouragement throughout the project.

I would like to recognize the joint support from the University of Ottawa and Tampere University for giving me the great opportunity to visit Tampere University in Finland twice in January 2018 and August-September 2018, respectively as an invited visiting research student as a recipient of the University of Ottawa International Experience Scholarship. I would also like to thank SPIE for awarding me the prestigious SPIE Education Scholarship award for my contribution towards optics and photonics.

I am grateful to Prof. Jean-Michel Menard, Dr. Jeremy Upham, Dr. Robert Fickler, Dr. Daniel G. Espinoza, Dr. Lambert Ginner, Dr. Enno Giese, for all of their kind academic, administrative and other supports.

I am also grateful to Mr. Hugo Begin, Ms. Gloria Kaneza and Ms. Deniz Akmaner for all of their kind academic, administrative and other supports.

I will always remember Asad A. Tahir, M. Zahirul Alam, Payman Rasekh, Prova C. Gomez, Shayan Saedi, Sisira Suresh, Kaustubh Vyas, and all other

CERC members for becoming my friend and making my life cheerful at the University of Ottawa.

It was also pleasuring for me to meet some nice people in Tampere University, Finland; namely Prof. Humeira Chaglayan, Timo Stolt, Antti Kiviniemi, Sreekanth Perumbilavil, Zahra Eslami, Shanti Toenger, Saiful Islam Sunny, Nekhel, Pooja Barma and few other people whose names I cannot remember right now.

I recognize with great significance the enormous help and support during my application in Master's abroad from Prof. Atiqur Rahman, Lecturer Ms. Sanjida Moury, Prof. Rashedul Hasan, and my very supportive friend-comementor Md Ibrahim Khalil Salman from North South University, Bangladesh.

Last but not least, I express my life-time gratefulness to my beloved mother Sufia Alam and father Md Shamsul Alam, my sister Shammi Akhter and brother-in-law Nisher Khan, my nephew Shafin Khan and niece Nahian Mahzabeen; who are my true inspiration and whom I miss every moment in my life. Also, I am thankful to my grandmother Abeda Hauque, my sister's father-in-law Md Kashem Khan, my all uncles and aunts, and rest of the relatives from my huge family.

May Allah bless all of us with peace! Ameen!

Dedicated to my mother, father, sister and her family.

Contents

List of Figures

"Allah is the Light of the heavens and the earth.
The example of His light is like a niche within which is a lamp,
The lamp is within glass, the glass as if it were a pearly [white] star,
Lit from [the oil of] a blessed olive tree,
Neither of the east nor of the west,
Whose oil would almost glow even if untouched by fire.
Light upon light.
Allah guides to His light whom He wills.
And Allah presents examples for the people,
and Allah is Knowing of all things."
—— Al-Quran;
Chaper 24: An-Nur (Light);
Verse 35: Ayat An-Nur (The verse of light)

Chapter 1

Introduction

1.1 Light-matter interaction and nanophotonics

Light-matter interaction is one of the most significant phenomena in our daily life. Because of the inherent nature and consequence of light-matter interaction such as reflection, refraction, diffraction, *etc.*, image of any object can be formed away from the real object. Thus, the visual information of that object can be transferred from one place to another.

The science related to the physical properties of light is known as optics. Though the first thought on visual perception was given by Ptolemy during the Greek era, the precise fundamental concepts of geometrical optics were developed in the pre-medieval Islamic civilization mostly by Abu Sa'ad al-A'la ibn Sahl (on refraction) and Al-Hasan (Alhazen) ibn al-Hytham (on colors, vision, visual perception and reflection) [1], [2]. Their works later inspired others in the medieval period, and got maturity during the European renaissance in the hand of Newton (on corpuscular theory), Huygens (on wave theory), and Maxwell (on electromagnetic theory). While Huygens considered light as a form of wave, Newton believed light consisted of many particles (corpuscles). In the late medieval era, Maxwell came up with his electromagnetic theory. However, after the introduction of the concept of quantum mechanics by Max Planck in the advent of the modern age, the modern scientific community realized that light actually maintains a wave-particle duality in nature. In other words, light can simultaneously behave like waves and particles (the latter known as photons). On the other hand, bulk matter is also formed by the chemical bonding of numerous atoms and molecules. So in reality, during a macroscopic light-matter interaction process, the photons of light microscopically interact with the atoms

or molecules (they are also called particles) of a certain matter. This photon-particle interaction essentially governs the overall response of macroscopic light-matter interactions.

The discipline of knowledge ensuing over the 20^{th} century based on the physics of photons is known as photonics. As an obvious consequence, from the middle of the last century, modern civilization has observed a massive revolution in the discovery of lasers, optoelectronic devices and optical telecommunications. In addition, the advent of the state-of-the-art micro- and nano-fabrication system has pushed modern scientific research and industrial engineering towards the rise of integrated photonics-based devices, which found their position in computer and telecommunication systems. Sometimes a photonic structure needs to be made very small in size (which is often on the order of a few nanometers); the field of study related to that sort of photonic structures is also referred to as nanophotonics. Also, photonic structure is nano-sized, it may possess properties not found in the bulk material.

Thanks to the electron or photon carrier properties, semiconductor materials are also the materials of choice for optoelectronic and integrated photonic devices – such as light emitting diodes (LED), laser diodes, optical waveguides, photodiodes, charged-coupled devices (CCD), photovoltaic solar cell, photonic crystals and others [3]. The most common material among them is silicon (Si). In addition, the high nonlinear optical response of the semiconductor materials also makes them suitable for many applications [3], [4]. Some organic materials have been gaining popularity day-by-day as alternatives to their semiconductor counterparts [3]. Nowadays, photonic industries are rapidly growing all over the world.

Although it is assumed that the current technology has reached its zenith to fulfill almost all the requirements in our everyday life, the scientific quest never ceases to reveal the astonishing hidden beauties of nature. For example, while semiconductor materials are responsible for the development of the integrated photonic devices in the forms of light sources, waveguides or propagating channels, as well as detectors, they cannot replace the role of metals (*e.g.* bulk gold, silver, aluminum *etc.*) as reflectors. However, putting aside all the great benefits of the naturally available materials, the scientists acknowledge a big limitation. Although the photon-particle interaction naturally takes place in sub-atomic or sub-molecular level in naturally available materials, it is not possible to manipulate or tune the properties of light inside the material's structure. In other words, one would need to depend on the

inherent properties of the materials available in nature for any applications. This limitation prohibites the exploration of many unrevealed phenomena associated with light. For that reason, optical scientists and engineers seek to develop alternative ways to play with light-matter interactions artificially or in an engineered manner. Their tremendous interests and efforts eventually led them to develop the concept of artificially structured materials at the beginning of the 21st century, widely known as metamaterials.

1.2 Meta-structures

It was Victor G. Veselago who came up, for the first time, with the theoretical concept of a new and exciting idea in the late 60's – the idea of a material system with negative permittivity and negative permeability [5]. In other words, he proposed a material system with negative refractive index which could refract incident light in an opposite direction compared to the traditional refraction occurring in natural dielectric media. Although metals (more specifically, transition metals like gold and silver) exhibit negative electric permittivity in the optical wavelength range, it is not possible to find any material which has magnetic permeability with the negative sign, even with the value less than 1 [6].

At the early stage, Veselago's theoretical concept could not become of any significance. It was at the very beginning of the 21st century when Veselago's work was eventually able to draw the attention of Sir John B. Pendry, and took a new shape in his seminal paper where he showed how to form a negative-refractive-index perfect lens by creating artificial media from naturally available materials [6]. This revolutionary theoretical work shook the whole community [7], and the concept of metamaterials (greek meta = beyond the natural, or simply artificial) emerged. Following this, researchers in the field of electromagnetics and optics from every continent jumped on this topic to take the concept of metamaterials from the theory to the laboratory. The first one-and-half decades of the 21st century can be marked as the golden period of the academic research in metamaterials [8], [9].

The best way to form a metamaterial is to use transition metals (*e.g.*, gold and silver), widely known as plasmonic metals. The reason is straightforward: in the relatively high frequency ranges, plasmonic metals inherently possess negative pemittivity. The permittivity becomes positive and metals

behave like dielectrics in the frequency range larger than the plasma resonant frequency where inter-atomic transitions take place. Plasmonic metals in optical range are also called electric metamaterials since they need to be much smaller in size than the excitation wavelength to be able to excite their resonances [10]. A tiny metallic nanorod is a good example of this phenomenon. To achieve negative magnetic permeability, one just needs to bend a nanorod to form a split ring-like structure which introduces a circulating current along its length, thereby artificially producing magnetic permeability. Due to this reason, this kind of structural shape is known as magnetic metamaterial. The combination of both negative permittivity and permeability of the metamaterial turns it into an artificial negative-index medium.

As the nanofabrication techniques matured, the experimental works on optical metamaterials became possible in the laboratory environment. Since a single metamolecule exhibits very weak signal, it is necessary to form a whole array of identical metamaterials to enhance the signal. This approach gave rise to two-dimensional (2D) arrays of metamolecules called metasurfaces. The structural elements of metasurfaces are called either individual meta-atoms or metamolecules.

1.3 Plasmonics

In case of the plasma oscillation in a material, there are quanta of such oscillations called plasmons. The plasma state of a matter is the cloud of free electrons of that particular matter. In other words, when the cloud of free electrons oscillates collectively, the discrete number of the oscillation is called plasmons [11].

The plasmons can be coupled to photons of the incident light in the optical regime. As a consequence of this coupling, a quasiparticle is created known as a plasmon polariton. Since free electrons are only available in metals (conductors) and semiconductor materials, plasmons and plasmon polaritons are only associated with them. Based on the size and geometry of the metals, there are two types of fundamental excitations in metals: (1) surface plasmon polaritons (SPPs) and (2) localized surface plasmon resonances (LSPRs) [11].

Surface plasmon polaritons (SPPs) are infrared or visible-frequency electromagnetic waves that travel or propagate along a metal–dielectric or metal–air

interface. The term "surface plasmon polariton" explains that the wave involves both charge motion in the metal ("surface plasmon") and electromagnetic waves in the air or dielectric ("polariton"). As the wave decays exponentially away from the surface of the metal, SPPs are also known as evanescent waves.

On the other hand, when light is incident onto a metallic particle, conduction electrons near the metal surface can couple with the incident electric field, and become collectively displaced from their equilibrium positions with respect to the core ions. This collective motion or plasma oscillation of electrons can be described as a lorentzian oscillator or resonator, and is called a localized surface plasmon resonance (LSPR). It causes a polarization of the particle (with the displacement amplitude called polarizability) and generates a depolarizing field that acts as a restoring force. Some unique properties of the LSPRs are listed below.

- The local electromagnetic field near the nanoparticles can be significantly enhanced leading to stronger light-matter interactions.
- The field can be localized down to the sub-wavelength scale, which makes it possible to control light-matter interactions at distances shorter than the traditional diffraction limit.
- The occurrence of LSPs and their resonances are influenced by the nanoparticle size, shape and environment, thus providing opportunities for various applications ranging from near-field microscopy to sensing.

Thanks to the unique characteristics of metal plasmonic nanoparticles, they have been proposed as prominent materials of choice for diverse potential nanotech applications [9]. In addition, they are the key building blocks of any plasmonic metasurfaces [12]. Metamaterials inspired optical nanocircuits [13], *etc*. Therefore, they are often called as "meta-atoms" or "metamolecules" [9].

The resonant pattern of LSPs depends on the size and geometry of individual metamolecules. To analyze the linear characteristics of plasmonic metamolecules with different shapes, a well-known simple but crude formalism has been proposed known as equivalent *RLC* circuit model. [12]–[14].

The early studies on plasmonic metamaterials comprised design methodology and controlling the localized surface plasmon resonance associated with

the individual metamolecules. Later, many research groups explored practical applications of the metasurfaces. Because of their unique characteristics, ability to manipulate the properties of light structurally, and especially their high nonlinear optical responses, plasmonic metamaterials were deemed to hold promise in many applications, such as chemical and biological sensing, filtering, resonators, efficient second- and third-harmonic generation processes, lasing and many others [15], [16]. Plasmonic nanoparticles have high intrinsic absorption losses affecting the quality of their localized resonances. Therefore, they have been considered practical for a limited number of applications such as biosensing. However, the nonlinear optical response of silver and gold is significantly higher compared to that of other materials (*e.g.*, silicon), which makes plasmonic nanoparticles superior for nonlinear optics applications [4].

1.4 Nonlinear optical processes

In the process of light-matter interactions, each atom or molecule becomes polarized by the electric field of the incident light. In general, the induced polarization of the material depends upon the electric field strength of the incident light. This dependence can be represented in the form of a power series expansion [4]:

$$\begin{aligned} \tilde{P}(t) &= \epsilon_0 \chi^{(1)} \tilde{E}(t) + \epsilon_0 \chi^{(2)} \tilde{E}^2(t) + \epsilon_0 \chi^{(3)} \tilde{E}^3(t) + ... \\ &= \tilde{P}^{(1)}(t) + \tilde{P}^{(2)}(t) + \tilde{P}^{(3)}(t) + ... \end{aligned} \tag{1.1}$$

where the first term corresponds to the linear relationship between the electric field strength and the induced polarization through a constant of proportionality called the linear susceptibility of the material. In the case of single atom or molecule, it is called induced dipole moment per unit volume. Other terms in the equation describe the second- and third-order nonlinear relationship through nonlinear susceptibility of the material. This quadratic and higher-order dependence of the induced polarization upon the strength of the electric field is the base of all nonlinear optical phenomena. It should be understood from the relationship that optical nonlinearity is not a characteristic of light itself. It is the manifestation of light-matter interaction that depends on the optical properties of the medium interacting with the incident light.

It is evident from the equation that in order to induce and polarize the matter nonlinearly, one needs to enhance the strength of the incident electric field. That is why, it is highly desirable to use a laser source for the observation of the nonlinear optical phenomena. A year later after the demonstration of the first laser by Mainman in 1960 [17], Franken, *et al.* successfully observed second-harmonic generation using a laser source [18].

The efficiency of the nonlinear optical processes is largely dependent on the type of materials and their inherent nonlinear optical response. The typical nonlinear optical phenomena are: (1) second-harmonic generation (SHG), (2) third-harmonic generation (THG), (3) sum-frequency generation (SFG), (4) difference-frequency generation (DFG), (5) optical rectification (OR), (6) saturable absorption, (7) two-photon or multiphoton absorption, (8) stimulated Raman Scattering, (9) self-focusing, *etc*.

1.4.1 Macroscopic and microscopic nonlinearity

The susceptibility of a material is a quantity that provides information about how the material becomes polarized in response to the strength of an external electric field. In the case of individual atoms or molecules, this quantity is expressed as polarizability, where the polarization of individual atoms or molecules is considered as the induced dipole moment. In the nonlinear regime, these quantities are simply replaced by the terms nonlinear susceptibility and hyperpolarizability for macroscopic and microscopic interaction, respectively.

The quantities of both the linear and nonlinear susceptibilities of a dielectric material (or polarizability and hyperpolarizability of an atomic or moleculer system) can be found theoretically by simply comparing the system with a mass-spring resonator, which is known as the Lorentz model of atoms. The limitation of the model is that it is only appropriate for bound electrons associated with dielectric and metallic atoms or molecules, but cannot be applied to free electrons of metals. Also, those quantities for metals are highly frequency-dependent in optical regime due to the dispersion. Although Drude or Drude-Lorentz model provides a theoretical expression for the polarizability of metallic nanoparticles, to calculate frequency-dependent optical permittivity of metal, one generally needs to perform numerical simulations. Such a computation is very bulky in the nonlinear optical regime.

After the rise of plasmonic metamaterial, researchers have developed an efficient way to calculate linear optical properties of metallic nanostructures by comparing them with an electrical resonator system widely known as *RLC* resonator or oscillator (where *R* = resistor, *L* = inductor and *C* = capacitor) [14], [19], [20]. It can be considered as a counterpart of the mass-spring oscillator, but for free electrons of plasmonic nanoparticles or metamolecules only. However, to best of our knowledge, there is no work available yet which extends this *RLC* circuit model to analytically express the nonlinear optical response characteristics of a metallic system. The probable reason might be the lack of model describing the nonlinear optical coefficients associated with free electrons. Indeed, there is no model comparable in simplicity and convenience to Miller's rule [21], which is only applicable to the nonlinear coefficients associated with the bound electrons. Here, we point out this issue and attempt to address it by considering the case of an individual plasmonic metamolecule in this thesis work.

1.4.2 Cascaded nonlinearity

Nonlinear optical interactions generally suffer from low efficiency due to the low values of the nonlinear susceptibilities of optical materials. The higher the order of the nonlinear optical effect, the weaker is the generated nonlinear optical signal. As the result, the detection of the direct higher-order nonlinear optical processes (such as, *e.g.*, third-harmonic generation) is very difficult.

One way to enhance the values of the higher-order nonlinear susceptibilities is to cascade the contribution from the comparatively stronger lower-order nonlinear responses [22]–[27]. Cascaded contributions of the lower-order nonlinear optical processes to the higher-order nonlinear effects has been shown to result in the stronger higher-order nonlinear optical signal because the lower-order nonlinear susceptibilities are several orders of magnitude stronger than the higher-order susceptibilities [27]. Therefore, cascaded nonlinear optical effects have been considered as practical means of generating higher-order harmonics.

1.5 Nonlinear response of plasmonic metamolecules

The nonlinear optical response of individual atoms can be understood by creating a simple analogy between the bound electrons and a mass-spring anharmonic oscillators [4], where the nonlinear displacement of the bound electrons with respect to the positive core ions plays a major role. However, that analogy does not allow one to take into account the contribution of free electrons in the case of plasmonic metals. When a wave of light impinges on a plasmonic metamolecule, the free electrons near the closed surface of the metal-dielectric interface begin oscillating collectively and coherently, giving rise to a resonance known as localized surface plasmon resonance [11]. The plasmonic excitations dramatically enhance the local field. And as the optical nonlinearity scales with the strength of the electric field, plasmonic effect can also significantly enhance the intensity of the nonlinear optical interaction [15]. Promising applications justify the interest in studying nonlinear optical effects in plasmonic metamolecules, which is the subject of focus in the field of nonlinear plasmonics.

To understand physical origin of plasmonic nonlinear optical effects, different numerical methods have been utilized including hydrodynamic models, nonlinear scattering theory, *etc.* [21], [28], [29]. These models often require time-consuming numerical computations, such as the finite-difference time-domain methods (FDTD). Nevertheless, thay are very effective for the above-mentioned tasks.

1.6 Plasmonic surface lattice resonances

Plasmonic metamolecules, placed in close proximity with respect to each other, extibit interaction in the near-field region [9], [16]. Because of the hybridization of the identical LSPR of the adjacent metamolecules, spectral position of the LSPR is either blue- or red-shifted, and its lineshape splits. Through this hybridization process, Fano-like asymmetric modes/resonances with narrower linewidths appear from the split lineshapes. However, these modes cannot be easily excited by an incident light, and are thus termed dark modes.

If plasmonic metamolecules are arranged in a random array, scattered fields from the surrounding metamolecules act on each individual metamolecule.

The effects of the average scattered fields are negligible as their phase are mismatched. However, when many identical plasmonic nanoparticles are periodically arranged to form a metasurface, the particles can become optically coupled near the diffraction orders (DOs) of the plane of the array associated with the lattice and form a new hybrid mode, which is known as a plasmonic surface lattice resonance (SLR) [16], [30], [31]. The wavelength of an SLR is dictated by the periodicities of the lattice, P_x or P_y, in the plane of the metasurface, as well as the refractive index of the surrounding (homogeneous) medium n.In a periodic array, the scattered fields acting on individual metamolecules are phase-matched and in phase with the incident light. These phase-matched scattered fields can oppose the damping of the plasmon resonance of an individual single metamolecules [16], [32]. When metamolecules are periodically arranged in a large array, the linewidth of LSPRs coupled with DOs goes down to a few nanometers, resulting in an enhancement in the quality- or Q-factor. Physically, it dramatically increases the absorption and enhance the local fields near the edge of the individual metamolecules.

Generation of a hybrid mode of plasmon resonance with narrower linewidth was first predicted by V. Markel in 1993 [33]. This prediction was followed by the work of Zou, performed in a 1-D chain of plasmonic nanoparticles *et al.*, published in 2004 [34]. In the latter work, the discrete-dipole approximation (DDA), also known as coupled-dipole approximation (CDA) method (developed by Purcell and Pennypecker [35]), was used to understand the appearance of SLRs. In 2005, Markel came up with another numerical method called dipole sum approximation (DSA) [36].

The first successful experimental demonstration of SLRs appearing in the near-infrared spectral range from a periodic plasmonic metasurface was reported in 2008 by Augie, *et al.* [30]. The authors pointed out that collimation of the incident beam plays crucial role in exciting a narrowband SLRs, since the collimated light couples with only one DO, thereby preventing the broadening of the linewidth of SLRs.

After the experimental demonstration of SLRs, the subject attracted a lot of attention of researchers, and it still remains one of the most active sub-fields in plasmonics. Different groups have been focusing on increasing the Q-factor of SLRs both theoretically and experimentally [37]–[39]. While there exist some theoretical works that suggest that the Q-factor can be enhanced to the level of over 10^3 [39], [40], experimentally, it never crossed the limit

of more than a few hundreds [37]. The reason was explained by Rodrigues, *et al.* [32], who suggested that the periodicity and the overall array size both contribute to an increase in the Q-factor. Their prediction is also supported by DDA and DSA models, where one can fix the number of metamolecules in the array [41]. This option is unavailable in FDTD simulations [39], [40] where one assumes an array of infinitely large size by applying periodic boundary condition. Torma's research group worked both on theory and experiment [31] as well as applications of SLRs such as lasing [42]–[44]. SLR also received attention in other works in the contemporary period. Different mechanisms of enhancing Q-factor of SLRs have been proposed recently, though they lead to the values of Q-factor not greater than 300 – 500 [37], [39].

Although there were many studies on linear aspects of SLR [39], [41], [45]–[52], very few works have been published on the impact of SLR on the nonlinear optical processes. It was proved earlier that LSPRs can enhance nonlinear optical processes [15]. The same should also be true in case of SLRs, but with a much higher performance, thanks to its relatively large Q-factor (compared to that of LSPRs). Some studies have been performed by Kauranen's and Elenbogen's groups [53]–[56] where the enhancement of second-harmonic generation (SHG) using SLRs was considered.

Very recently, Huttunen, *et al.* [56] theoretically demonstrated that SLRs can be used to enhance the nonlinear optical processes such as SHG, THG, SFG, DFG, and THG via cascaded SHG. In the paper, they considered a periodic 2D metasurface with the SLR around 750 nm. Specifically, they showed that, if a beam of light with the fundamental wavelength of 1550 nm falls onto an array of plasmonic metamolecules at normal incidence (z-axis), then SHG in the spectral range around 750 nm appears to be significantly enhanced. Moreover, it significantly modifies THG signal through cascading with the fundamental frequency component.

1.7 Coupling of localized surface plasmon resonance with Fabry-Perot microcavity

Schmidt, *et al.* [57] experimentally showed how to generate multiple norrow-band resonances on the basis of an LSPR by hybridizing the LSPR of individual nanoparticle with the Fabry-Perot (F-P) resonance originating from

a microcavity beneath the nanoparticle. Coupling between LSPR and F-P modes allows one to excite hybrid plasmonic supermodes: the incident light becomes localized within a small volume in the proximity of an individual nanoparticle, and gets redirected into the F-P microcavity modes. Inside the F-P cavity, that redirected light circulates. During this process, a portion of the light gets transferred out of the cavity modes back into the LSPR and is then scattered away from the nanoparticle [57].

1.8 Scope of the thesis

As discussed above, arrays of metamolecules hold promise for many applications. Specifically, they have potential to be used for enhanced nonlinear optical effects. While plasmonic metasurfaces are generally lossy and their localized resonances have relatively low Q-factors, the collective resonances of plasmonic metasurfaces exhibit an order-of-magnitude higher Q-factors compared to those of the localized resonances. It has been shown that the surface lattice resonance could result in orders-of-magnitude enhancements of nonlinear optical interactions in plasmonic nanoarrays [56].

Thanks to their design flexibility, plasmonic metasurfaces could provide a good test bed to create the conditions for exploring the cascading in nonlinear optics. For that, one needs to properly design an array of metamolecules to enhance the cascading phenomenon. This can only be done if one knows the values of nonlinear susceptibilities of individual metamolecules of the arrays. Numerical tools can be suitable for this task. On the other hand, such tools are typically computationally intensive and do not provide an intuitive answer with a clear physical picture. The primary goal of this thesis is to develop a simple analytical model capable of predicting the values of the nonlinear hyperpolarizabilities of plasmonic metamolecules based on the knowledge of their shapes, dimensions, and material.

Prior to analyzing nonlinear optical properties of plasmonic metamolecules, we looked into developing an analytical model capable of predicting their linear optical response. Specifically, we considered a model based on the equivalent electrical lumped circuit elements (resistor, capacitor, inductor), which is called RLC oscillator model. Although this model was found in literature mainly for U-shaped split ring resonators and cylindrical nanorods [19], [20], other shapes have not been explored to date. Moreover, the existing

models do not account for optical nonlinearity at the visible spectral range. This thesis can thus be divided into three distinct subtopics: (a) reformulation and generalization of the *RLC* model to describe a plasmonic metamolecule of an arbitrary shape and extension of the model to the nonlinear optical regime; (b) experimental measurement of the nonlinear hyperpolarizabilities of individual plasmonic metamolecules and comparison of their values with the predictions of the analytical model; and (c) experimental measurement and numerical modelling of high-Q surface lattice resonances of plasmonic metasurfaces. These objectives represent crucial milestones towards the ultimate goal of this research: the realization of plasmonic nanoarrays for the observation of microscopic cascading effects in nonlinear optics.

1.9 Structure of the thesis

The purpose of this chapter (Chapter 1) of the masters dissertation was to place this research in a conceptual context. We introduced the relevant basic concepts and discussed the importance of plasmonic metamaterials in the linear and nonlinear photonics. Moreover, we outlined the specific field of study and explained how the objectives of this thesis contribute to the ultimate research goal to create a test bed for microscopic cascading in nonlinear optics.

In chapter 2, we introduce the linear *RLC* resonator circuit model, and apply it to describe the linear optical response of a basic metamolecule structure called plasmonic nanorod. We show that, using *RLC* model developed for a plasmonic cylindrical nanorod (the simplest form of any nanorod-like structure), it is also possible to analyze the linear optical response of more complex but similar structures, *e.g.*, rectangular nanobar and triangular elongated nanoprism.

In chapter 3, we extend our *RLC* circuit model to the nonlinear optical regime and derive microscopic nonlinear hyperpolrizabilities of individual metamolecules. The analytical result is then verified with the second harmonic generation experiment performed in an aperiodic array of triangular metamolecules.

Chapter 4 is dedicated to the design of a 2D plasmonic metasurface to study hybrid plasmonic-cavity multiple band resonances combined with a high-quality-factor surface lattice resonance (SLR). The target wavelength of our

SLR was 1550 nm, whereas the main LSPR wavelength was 1100 nm. We experimentally observed the multiple sharp resonances arising from the coupling between the localized surface plasmon resonance (LSPR) and the SLR.

Chapter 5 describes the most exciting contribution of this Master's dissertation. Here we experimentally demonstrate ultra-high-quality-factor plasmonic SLR from a 2D plasmonic metasurface. The target wavelength of the SLR was 1550 nm. We were able to achieve record high Q-factor close to 1000.

The summary and conclusions of the full dissertation are presented in Chapter 6, and are followed by the discussion on what we could explore in the future having the benefits of the work done in this thesis.

Chapter 2

Plasmonic resonance analysis using LC lumped elements

2.1 Introduction

In Radio-frequency (RF) and microelectronics, the concept of a "circuit" describes a relation of an electric current (flow of a fixed amount of charges or electrons in opposite direction) with an electric potential established through the functions of "lumped" elements such as resistor, inductor, capacitor, diode, *etc.* [13]. A resistor R (also called insulator) is responsible for introducing the loss (by prohibiting or limiting the current) in a circuit. An inductor of the inductance L is mechanically formed by a metal (conductor) coil to store energy in a magnetic field as the current passes through it. A capacitor with the capacitance C, on the contrary, stores the energy in an electric field through the electric potential across two oppositely charged metallic surfaces separated by a dielectric medium. This separation can either be a gap between two detached metal plates or two opposite facets of a metal sheet/rod (placed in a dielectric medium) charged by electrons of opposite signs.

Now consider a circuit formed by at least one inductor and one capacitor connected in series (series circuit). If an external potential energy *e.g.* voltage of an alternating current (A.C. current) is applied to this circuit formation, at first the inductor will allow the current to pass through it, then it will create a circulating magnetic field surrounding itself orthogonal to the direction of the current. This way it will absorb the energy from that passing current and store in that created magnetic field. Note that no voltage potential is created across the inductor during this process. After a certain amount of time, the current will start to leave the inductor and move towards the capacitor. During this period, while the inductor will start to release its stored energy, the

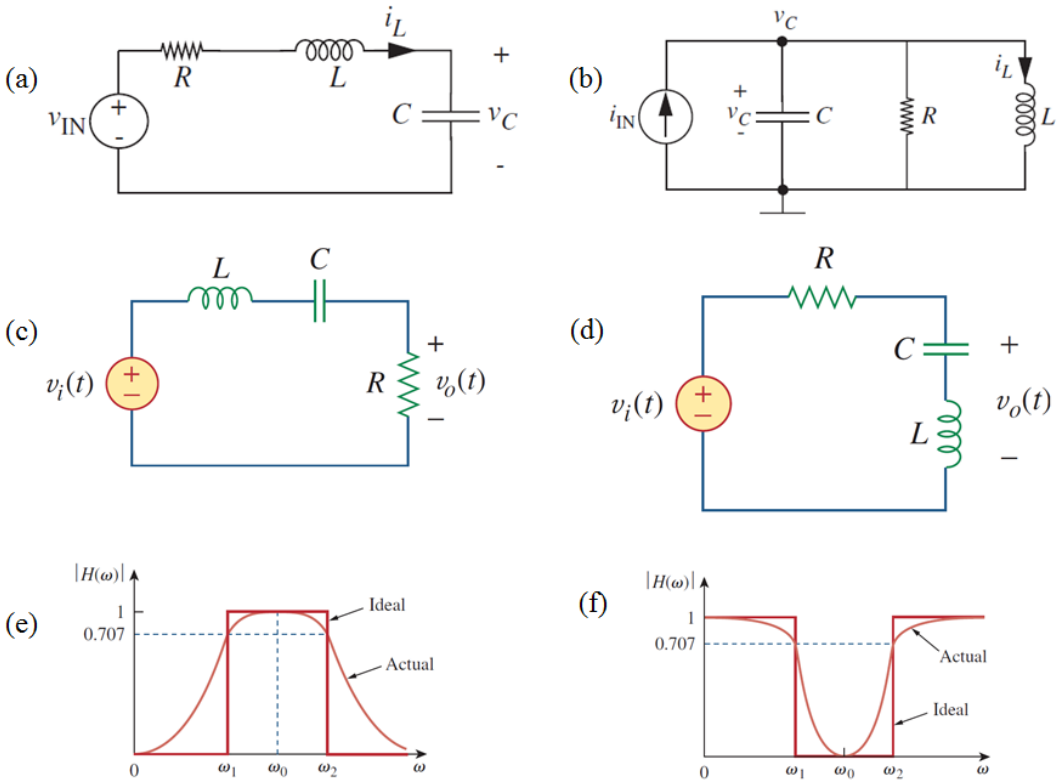

FIGURE 2.1: Schematics of (a) a series *RLC* circuit, (b) a parallel *RLC* circuit, (c) a band-pass filter, (d) a band-stop (notch) filter. Ideal and actual frequency responses of (e) a band-pass filter (f) a band-stop (notch) filter [58], [59].

capacitor will start to store energy in a form of electrostatic field created by its oppositely charged two metal plates or ends. Note that no current can pass through the dielectric material of the capacitor; so only a distributed voltage is created across the two plates or ends of the capacitor, which is called distributed capacitive voltage. This whole process will be completed in one cycle of the current flowing in only one direction. In this cycle, we can see that energy is being transferred from the inductor to the capacitor. When the next cycle of the current will start (flowing in opposite direction), the capacitor will then start to dissipate energy to the circuit by discharging the accumulated charges on its two plates or ends, and allow to pass the current towards the inductor. Then the inductor will again store the energy in the same way described above. This way, the cycle of the current passing in alternate direction will be completed, where the energy is handed-over from the capacitor to the inductor in a reverse process.

This restoring-dissipating process between the inductor and the capacitor will continue as long as the external potential with A.C. current source will be applied continuously. The repeated back-and-forth transferring of the energy between the inductor and the capacitor will create an oscillation of the stored energy of the circuit. Now, there is a very certain moment when the magnitude (the amount) of the stored energy in both the inductor and the capacitor will become equal. This moment, the amplitude of the overall oscillating energy stored in the circuit will reach its zenith level and create resonance. At the moment, the inductor and the capacitor are said to reach their resonant condition, and the overall circuit is called the resonator. From the description of the origin of the electromagnetic resonance in the circuit, it is obvious that to form a resonator, a circuit must contain both an inductor and a capacitor. Therefore, a resonator circuit is also referred to as LC resonator circuit [58], [59].

However, in reality, such a circuit experiences resistive loss while the current passes through it due to the inherent absorptive loss of the connecting metal wires. When the electrons flow (conventionally in the opposite direction of the current) pass through the metal, they collide with the free electrons near the surface of the metal. Because of this collision, some of the energy will turn out to heat and dissipate or loss in the surrounding environment. Therefore, practically one cannot ignore the presence of the resistivity in a circuit denoted by R, which is responsible for the damping or decay of the energy with a damping factor or coefficient $\gamma = 1/\tau = R/(2L)$ or $\gamma = 1/(RC)$

($\tau = RC$ is the time constant [59]). For that reason, unlike ideal condition, instead of LC circuit, we have to design and analyze an RLC resonator circuit [demonstrated in Fig. 2.1(a)]. Let us remind again that, throughout the above discussion, we only consider a series LC or RLC circuit. A similar resonance can also be observed in a parallel combination of the lumped elements [see Fig. 2.1(b)], but since that discussion is beyond the scope of this thesis, we omit it here.

Naturally, the oscillation of the energy between the inductor and the capacitor in a LC or RLC circuit is not steady-state, but transient over time. The current inside the inductor and the voltage inside the capacitor accumulated and dissipated gradually over the certain period of time, respectively. Therefore, the relationship between the voltage and inductance (through the current) as well as the relationship between the current and capacitance (through the voltage) mathematically follow the time-dependent differential and integral forms, respectively (which we will see later). Since an LC or an RLC resonator circuit consists of these two transient lumped circuit elements, such type of circuits is known as second-order differential circuits because they can be described by a second-order differential equation [58].

By definition, any cyclic oscillation process has a certain angular frequency (or wavelength) associated with it. The corresponding frequency (or wavelength) is known as the resonant frequency (or wavelength) of the oscillation. Back to the RF or microelectronics, an RLC resonator circuit can be implemented to form a band-pass or band-stop (notch) filter circuit [see Fig. 2.1(c) and (e), respectively], which may allow or restrict the passing of the applied wave or signal by the circuit in a certain range of frequencies (or wavelengths) [see Fig. 2.1(d) and (f), illustrating the frequency responses of the band-pass and band-stop filters, respectively]. Therefore, in case of any band-pass or band-stop (notch) filter, the resonant frequency (or wavelength) is also known as center frequency (or wavelength). Note that, the absence of either of L or C will turn the circuit into either low-pass or high-pass filter. Again, we are omitting the discussion since it is not relevant to the focus of the thesis.

Next, it is important to consider in which situations a RLC resonator circuit acts as a band-pass and as a band-stop filter. When an input external voltage of an A.C. signal is applied across the series RLC circuit, the output taken off the resistor allows to pass the signal with the frequency corresponding to the resonance or center frequency of the circuit, which corresponds to band-pass

filtering [Fig. 2.1(c and e)]. On the other hand, if the output is taken off the series combination of LC, it restricts/stops the signal with the frequency close to the circuit resonance. This corresponds to band-stop filtering [Fig. 2.1(d and f)]. In such a way, the filtering process depends on where the output is being taken off. Physically, since L and C store or trap energy of an applied signal matching the resonant conditions, that energy cannot get released to the output. The situation becomes opposite in case of taking the output from R.

Let us now shift our focus from RF/microelectronics domain to optical frequency or wavelength regime. We already discussed in Chapter 1 that a plasmonic nanoparticle or metamolecule can be used to control light at the nanoscale. Individual plasmonic metamolecules confine or "trap" the incident light near the surface of the metal-dielectric interface using localized surface plasmon resonances (LSPRs) of the cloud of free electrons. Therefore, the metamolecules do not allow to transmit the energy of the on-resonance incident light (similar to a band-stop filter). Because of such similarity, plasmonic metamolecules can be considered as an optical analog of an LC or RLC resonator. Physically, when illuminated by light with a certain polarization orientation, a plasmonic metamolecule at first becomes polarized: the free electrons get displaced from their original positions. The two opposite facets/ends of the nanoparticle become oppositely charged: one end accumulates free electrons and becomes negatively charged, while the other end develops a deficit of free electrons and becomes positively charged. In such a way, the nanoparticle or metamolecule turns into a capacitor with the capacitance C, storing the electrostatic potential energy near its ends. As mentioned before, depending on the geometry or shape of the metamolecule, the mathematical interpretation or expression of C may vary. For example, in an earlier work [19], the capacitance of a U-shaped split-ring resonator (U-SRR) was deduced based on the similarity in physical shapes of a U-SRR and a parallel-plate capacitor:

$$C = \pi\epsilon_0\epsilon_{\mathrm{r}}\frac{l_y l_z}{g} \qquad [\mathrm{F}]. \tag{2.1}$$

Here ϵ_0 and ϵ_r are the vacuum permittivity (8.85×10^{-12} F/m) and the relative permittivity of the surrounding medium, l_y and l_z are the width and height of the parallel-plates-like legs and base of the U-SRR, and g is the separation gap between the legs [shown in Fig. 2.2(a)].

But in case of a cylindrical nanorod [shown in Fig. 2.2(b)], there is apparently no gap, and C takes a different form. Each facet of the cylindrical nanorod can be approximated as a circular-disc capacitor with the capacitance in the form [20]

$$C = 2\pi\epsilon_0\epsilon_r r_0 \qquad [\mathrm{F}], \tag{2.2}$$

where r_0 is the radius of the disc [20]. In both equations (2.1) and (2.2), as well as in many following equations, we explicitly show the physical units in the square brackets following the equations. These are used for parameter estimates later.

According to ref. [20], after the metamolecule becomes polarized in accordance with the polarization direction of the applied optical field, the free electrons accummulated in one end then start flowing towards the other end of the metamolecule; by convention, this will initiate the flow of the current in opposite direction. This current will create a circulating magnetic field in the orthogonal direction. This phenomenon will turn this metamolecule into an inductor, which will store energy in form of a magnetic field in its surrounding region. Notice that by the gradual change of the status of the nanoparticle from a capacitor to an inductor will cause the transferring of the energy once stored in an electrostatic field to a magnetic field. This phenomenon is called self-inductance and is described by the associated inductance L_{self} which has the form [20]

$$L_{\mathrm{self}} = \frac{\mu_0 l_x}{2\pi} \log \frac{l_x}{2r_0} \qquad [\mathrm{H}], \tag{2.3}$$

where l_x is the length of the nanorod in x-direction, and μ_0 is the vacuum permeability (1.257×10^{-6} H/m).

Up to this point, the expressions for C and L were similar to those provided for a capacitor and inductor in electromagnetic theory. But one thing is still missing: at the nanoscale optical regime (where the sizes of the nanoparticles are much smaller compared to the wavelength of light), a change in electromotive force (emf) due to alternating electric fields is opposed by the inertia of the charge carriers (free electrons) with mass m. These charge carriers travel at constant velocity v which requires a finite time to accelerate them. During the travelling the free electrons gain the kinetic energy U_{kinetic}, which creates the kinetic inductance L_{kinetic} [14], [19], [20]. Mathematically, the kinetic energy can be expressed in the form described below:

$$U_{\mathrm{kinetic}} = (\frac{1}{2}mv^2)(nl_xA) \qquad [\mathrm{J}]\,, \tag{2.4}$$

where n is the density of the free electrons, and $A = \pi {r_0}^2$ is the cross-sectional area of the cylindrical nanorod. Now, considering the fact that the current $I = qnvA$ (where q is the electron charge, we can derive the kinetic inductance for the cylindrical nanorod from the following relation [20], [60]:

$$\frac{1}{2}L_{\text{kinetic}}I^2 = (\frac{1}{2}mv^2)(nl_xA) \qquad [\text{J}]\,, \tag{2.5a}$$

$$L_{\text{kinetic}}q^2n^2v^2A^2 = mv^2nl_xA \qquad [\text{J}]\,, \tag{2.5b}$$

$$L_{\text{kinetic}} = \frac{m}{ne^2}\frac{l_x}{A} \qquad [\text{H}]\,, \tag{2.5c}$$

$$L_{\text{kinetic}} = \frac{\mu_0}{\frac{ne^2}{m\epsilon_0}\epsilon_0\mu_0}\frac{l_x}{A} \qquad [\text{H}]\,, \tag{2.5d}$$

$$L_{\text{kinetic}} = \frac{\mu_0 l_x}{\frac{{\omega_p}^2}{c^2}A} \qquad [\text{H}]\,, \tag{2.5e}$$

where $\omega_p = 13.8 \times 10^{15}$ rad/s [61] is the plasma frequency of gold in the optical wavelength range, and the velocity of light is $c = 3 \times 10^8$ m/s. The total inductance L can be written as the sum of the two contributions:

$$L = L_{\text{self}} + L_{\text{kinetic}} \qquad [\text{H}]. \tag{2.6}$$

After the change of the polarization direction of light, the whole process is reversed, and a full cycle of alternating current in the metamolecule is completed in a similar fashion to a LC resonant circuit. When the energies stored in both the electrostatic field and magnetic field will become equal in magnitude, the metamolecule will exhibit LSPRs, which can verily be considered as a nanoscale optical analog of RF/microelectronic LC resonator.

Since a plasmonic metamolecule is made of metal, it possesses high intrinsic absorptive loss (*i.e.* due to high collision rate among the collectively oscillating clouds of the free electrons). This inevitable loss can be interpreted in terms of the resistance R, which will cause the damping or decay of the energy with a damping factor or coefficient $\gamma = 1/\tau = R/(2L)$ or $\gamma = 1/(RC)$, where $\tau = 2L/R = RC$ is the time constant [59]. In other words, a practical plasmonic metamolecule actually acts like a RLC oscillation circuit.

Due to the similarity between LSPR of plasmonic metamolecule and RLC resonance of a band-stop or notch filter circuit, they both exhibit similar resonant pattern in transmission (Lorentzian cup-like shape) and extinction

(Lorentzian bell-like shape). Further in this chapter, we will reproduce transmission pattern of a cylindrical nanorod by deriving its linear polarizability (and extinction coefficient from the linear polarizability) and using the expression of the capacitance C and inductance L given in [20], and then compare with numerical simulation. Next, we will modify the expressions of both C and L (henceforth the expression of linear polarizability) to make them applicable to other similar nanorod-like of structures such as symmetric rectangular nanobar. After that, we will analyze how the same expressions of both C and L can be used to determine the resonant wavelength of an asymmetrically shaped nanobar *e.g.* triangular nanobar (a.k.a. elongated nanoprism). The importance of the nanoprism stems from the fact that it lacks the center of symmetry and is thus expected to exhibit stronger second-order nonlinear optical interactions. In all cases, we assume that the light is incident in the normal direction (z-axis) and polarized along the x-axis.

2.2 LC-like resonances of plasmonic nanorods

In order to obtain the dependence of the transmission coefficient on the wavelength, we need to derive the linear polarizability for a nanorod from the RLC characteristic second-order differential equation. We start by assuming that an incident in normal direction field $\tilde{E}_{\text{inc}} = \tilde{E}_0 \exp(i\omega t)$ [volt/meter (V/m)] drives the circuit associated with the nanorod metamolecule by inducing an electromotive force $\tilde{\varepsilon}(t)$. Since the movement of the conduction electrons is damped by electron collisions, the produced current $\tilde{I}(t)$ (where the tilde denotes time-variable parameters) satisfies the following equation:

$$L\dot{\tilde{I}} + R\tilde{I} + \tilde{V}_C = \tilde{\varepsilon}(t) \qquad [\text{V}]\,, \tag{2.7}$$

where the dot denotes time derivative. Also, L [Henry (H)], R [Ohm (Ω)], and $\tilde{V}_C$ [volt (V)] are the distributed inductance, distributed resistance and the induced voltage across the distributed capacitance C [Farad (F)] of the circuit, respectively. By using the distributed capacitive voltage-capacitance relation $\tilde{V}_C = 1/C\,\acute{\tilde{I}}$, we can rewrite Eq. (2.7) as

$$L\dot{\tilde{I}} + R\tilde{I} + \frac{1}{C}\acute{\tilde{I}} = \tilde{\varepsilon}(t) \qquad [\text{V}]\,. \tag{2.8}$$

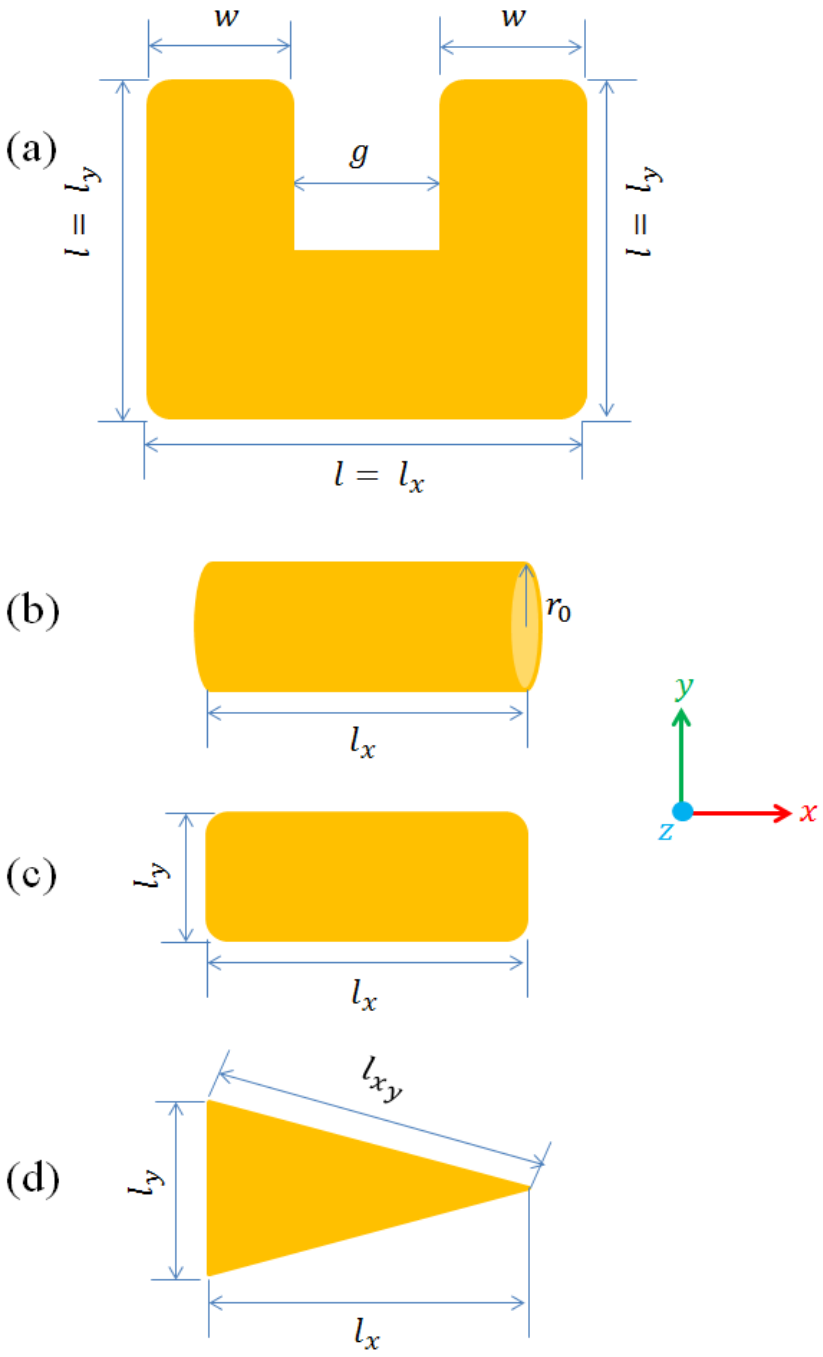

FIGURE 2.2: Plasmonic metamolecules of different shapes: (a) U-shaped split-ring resonator (U-SRR), (b) cylindrical nanorod, (b) rectangular flat nanobar, (c) triangular flat elongated nanoprism. The height h for (a) and l_z for (c-d) are measured in the direction perpendicular to the drawing's plane and are not visible on these 2D projection drawings.

Here, the acute sign on top of the current $\tilde{I}$ denotes the integral of $\tilde{I}$ over the time t. Then, using charge-current relation $\tilde{I} = \dot{\tilde{q}}$, we can transform Eq. (2.8) into a second-order linear differential equation:

$$L\ddot{\tilde{q}} + R\dot{\tilde{q}} + \frac{\tilde{q}}{C} = \tilde{\varepsilon}(t) \qquad [\mathrm{V}]\,. \tag{2.9}$$

From the previous discussion, we already know the relationship between R and the damping constant $\gamma = R/(2L)$ [per second (s^{-1})] [59]. So we can write Eq. (2.9) as:

$$L\ddot{\tilde{q}} + 2L\gamma\dot{\tilde{q}} + \frac{\tilde{q}}{C} = \tilde{\varepsilon}(t) \qquad [\mathrm{V}]\,. \tag{2.10}$$

We can divide Eq. (2.10) by L and obtain:

$$\ddot{\tilde{q}} + 2\gamma\dot{\tilde{q}} + \frac{\tilde{q}}{LC} = \frac{C}{LC}\tilde{\varepsilon}(t) \qquad [\frac{\mathrm{Coul.}}{\mathrm{s}^2}]\,. \tag{2.11}$$

Next, we can recall the relationship between the angular resonant frequency ω_0 and LC in the form of $\omega_0^2 = 1/(LC)$ [per second square (s^{-2})], and can re-arrange Eq. (2.11) as:

$$\ddot{\tilde{q}} + 2\gamma\dot{\tilde{q}} + \omega_0^2\tilde{q} = C\omega_0^2\tilde{\varepsilon}(t) \qquad [\frac{\mathrm{Coul.}}{\mathrm{s}^2}]\,. \tag{2.12}$$

The detailed form of the electromotive force $\tilde{\varepsilon}(t)$ [volt (V)] depends on the polarization orientation of the metamolecule. In case of any nanorod-like structure, if we assume that the metamolecule is polarized by the incident field along its length l_x (along x-axis), then the electromotive force $\tilde{\varepsilon}(t)$ can be expressed as $\tilde{\varepsilon} = -\tilde{E}_{\mathrm{inc}} l_x$. After substituting this expression into Eq. (2.12), we obtain:

$$\ddot{\tilde{q}} + 2\gamma\dot{\tilde{q}} + \omega_0^2\tilde{q} = -C\omega_0^2 l_x \tilde{E}_{\mathrm{inc}} \qquad [\frac{\mathrm{Coul.}}{\mathrm{s}^2}]\,, \tag{2.13}$$

which has a steady-state solution:

$$\tilde{q}(t) = q(\omega)\exp(-i\omega t) + \mathrm{c.c.} \qquad [\mathrm{Coul.}]\,, \tag{2.14}$$

where the amplitude $q(\omega)$ has the form:

$$q(\omega) = -\frac{C\omega_0^2 l_x E_{\mathrm{inc}}(\omega)}{D(\omega)} \qquad [\mathrm{Coul.}]\,, \tag{2.15}$$

here $D(\omega) = (\omega_0^2 - 2i\gamma\omega - \omega^2)$ is a complex denominator function related to the localized surface plasmon resonant frequency ω_0.

Since the induced electric dipole moment is usually calculated as the separation of positive and negative electrical charges within a system by a physical distance, here, we can define the induced dipole moment $p(\omega)$ to the charge $q(\omega)$ as:

$$p(\omega) = q(\omega) l_x \qquad [\text{Coul m}], \tag{2.16}$$

where we consider l_x as the separation distance between the positive and negative charges located at the opposite ends of the nanorod. At the microscopic level, the induced dipole moment p can be related to the linear polarizability α as:

$$p(\omega) = \epsilon_0 \alpha(\omega; \omega) E_{\text{inc}}(\omega) \qquad [\text{Coul m}]. \tag{2.17}$$

Substituting Eqs. (2.15) and (2.16) into Eq. (2.17), we can obtain the expression of the linear polarizability of the nanorod-like structure polarized along x-axis as follows:

$$\alpha(\omega) = -\frac{C\omega_0{}^2 l_x{}^2}{\epsilon_0 D(\omega)} \qquad [\text{m}^3], \tag{2.18}$$

or, taking into consideration the complex denominator, we can write:

$$\alpha(\omega) = -\frac{C l_x{}^2}{\epsilon_0} \frac{\omega_0{}^2}{\omega_0{}^2 - 2i\gamma\omega - \omega^2} \qquad [m^3], \tag{2.19}$$

here $\omega_0^2 = 1/LC$ is the resonant frequency of the equivalent circuit, $\gamma = R/2L$ (where $\gamma = 107 \times 10^{12}\ s^{-1}$ [61]) is the linear damping constant, and R is the resistance corresponding to the intrinsic absorption loss of the metal. The linear extinction coefficient, α_{ext}, can now be calculated by taking the imaginary part of the linear polarizability Im $[\alpha(\omega)]$.

At this point, let us recall the expression for the capacitance C of a cylindrical nanorod given by Eq. (2.2), and the expression for the inductance L given by Eq. (2.6) which were originally proposed in [20]. We calculated the frequency of light $\omega_0^2 = 1/(LC)$ for the cylindrical nanorod, and then took $\lambda_0 = 2\pi c/\omega_0$ to plot the transmission curve as a function of wavelength. We also assumed the relative permittivity of the surrounding homogeneous medium ϵ_r = 3.9 (for glass or fused silica), length along x-axis (in the polarization direction) l_x = 150 nm, and the radius of the cross-section in y-z plane r_0 = 25 nm (see Fig. 2.2(b)). We used this configuration to plot transmission $T = 1 - \alpha_{\text{ext}}$ shown in Fig. 2.3.

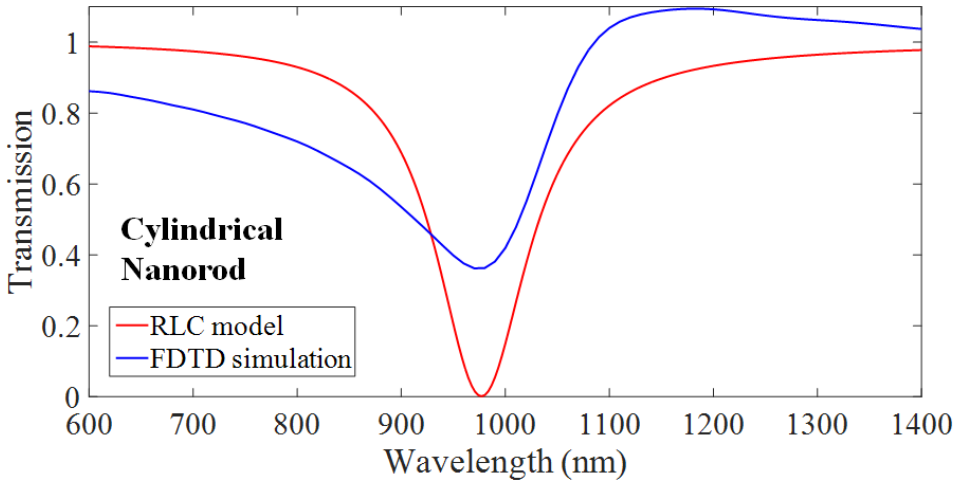

FIGURE 2.3: Comparison between the transmission of a cylindrical nanorod based on the RLC model and its FDTD simulations.

For the purpose of comparison, we performed FDTD simulation of LSPR of a cylindrical nanorod with the same configuration mentioned above using commercial Lumerical FDTD software. To simulate only a single nanoparticle, we applied the perfect matched layer (PML) boundary condition, which is impedance matched to the simulation region as well as the materials it contains inside it. It virtually creates an infinitely large background media surrounding the nanoparticle. Thus, ideally, it absorbs the scattered energy from the nanoparticle, and does not allow for reflections back to the nanoparticle. We compared the result of the simulated transmission with the analytical transmission spectrum, obtained for a cylindrical nanorod using Eqs. (2.2) and | (2.6) [see Fig. 2.3]. The comparison shows good agreement between analytical and simulated transmission in terms of the resonant wavelength λ_0.

Although the model proposed in [20] has been developed specifically for a cylindrical nanorod, in reality, it is difficult to fabricate a cylindrical nanorod lying on the substrate because of the curvature associated with its shape. Instead, it is much easier to fabricate a flat rectangular nanobar top on a flat substrate (to artificially fabricate a 2D metasurface) using electron beam (e-beam) lithography process. Thus, it would also be convenient to have such an equivalent *RLC* resonator model for a nanobar-like structure. In this chapter, one of our primary objectives is how to estimate the resonant wavelength and polarizability of a plasmonic nanobar by utilizing the similar expressions of L and C given above for a cylindrical shaped nanoparticle. However, for

the purpose of comparison, we also fabricated and characterized a real sample consisting of plasmonic nanobar, which we will briefly describe in the next section. [The fabrication has been done by Dr. Kashif M. Awan (former PhD student in our research group)].

2.3 Sample fabrication and characterization

The fabricated sample was comprised of a fused silica substrate patterned with four irregular arrays (randomly arranged nanoparticles in each array) of rectangular nanobars, which was later covered by index matching oil (refractive index n = 1.5) a microscope coverslip to make the surrounding dielectric medium of the plasmonic nanoparticles homogeneous. The irregularity in the nanoprisms positions was introduced on purpose to eliminate any lattice resonances (as the goal at this point is to measure the linear optical response of individual metamolecules in the metasurface). Other than their irregular position, for the sake of preserving the orientation of the nanobars with respect to the incident field polarization direction, all the nanoparticles were aligned with their longest dimension l_x along the x-axis in the laboratory coordinate frame (same as the polarization orientation of the incident field).

In the set of four arrays, the longest dimension l_x was gradually increased from 144 to the 177 nm with an increment of 11 nm from array to array, while l_z was fixed at 20 nm for all cases.

We measured the linear transmission spectra of all the arrays using the experimental setup demonstrated in Fig.2.4(b). We used a Tungsten-Halogen light as the light source with a very broad spectral range (400 – 2400 nm). We detected transmitted light using an optical spectrum analyzer (OSA) at the detection end. Since the incoming light from the source is unpolarized, a linear polarizer was placed after the collimation system to polarize the beam and to control the polarization orientation. Although light collimation is not mandatory to excite LSPRs, we collimated the incident beam using two lenses (4F system) for future purpose, which we will discuss in 4. The power of the input beam can also be controlled by the iris(es) placed in the path of the beam. The first iris just after the collimation system in Fig.2.4(b) was used to align the beam path with the array of interest and the detector.

Fig. 2.4(c) shows the transmission spectra of LSPRs of individual rectangular nanobars with different lengths l_x. From Fig. 2.4(c), we can easily realize

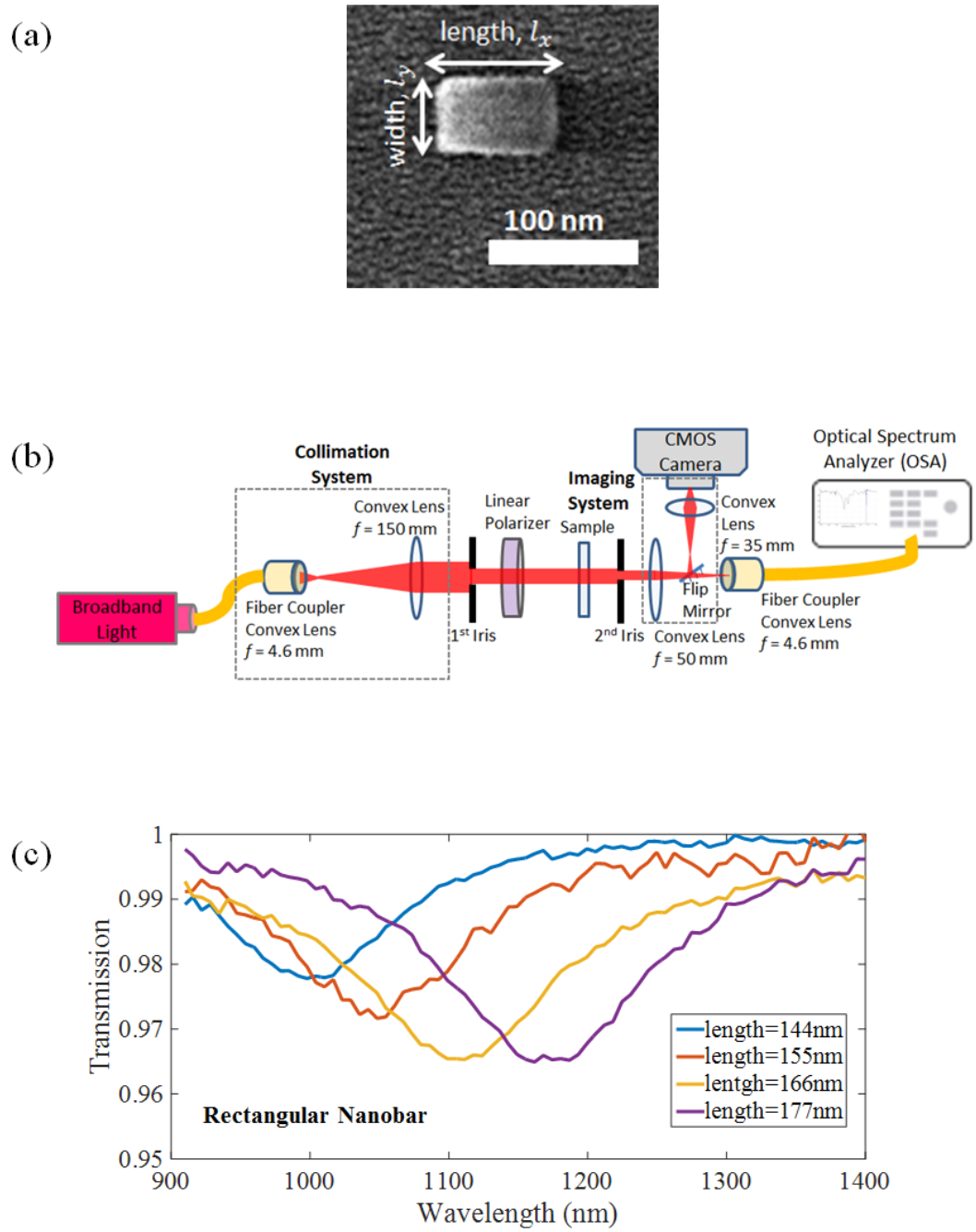

FIGURE 2.4: (a) SEM images of individual rectangular nanobar, (b) experimental setup for linear transmission measurements, (c) measured transmission spectra of the LSPRs of the rectangular nanobar with four different lengths along polarization of light.

that as the length of the nanobar increased, the resonant wavelength of the corresponding LSPR becomes red-shifted to the longer wavelength. Also, it is noticeable that, as the LSPR is red-shifted due to the length increase along the light polarization direction, its magnitude becoming enhanced, and its linewidth broadens.

2.4 Re-interpretation of C and L for plasmonic nanobar

Here we focus on developing a similar equivalent RLC model for a flat rectangular nanobar [shown in Fig. 2.2(c)], and obtain the value of the resonant wavelength analytically. As mentioned before, in case of a cylindrical nanorod, the facets of the nanorod were assumed to be circular disks with the radius r_0 so that the concept of circular-disk capacitor can be applied to express the capacitance C. To keep the conceptual aspect similar, we adapted the expressions of C and L in Eqs. (2.2) and (2.6), respectively, to the case of a rectangular nanobar with the folowing change. Instead of a circular disk with the radius r_0, we considered a rectangular plate with the width l_y along y-axis and height l_z along z-axis [due to the similarity in shape with a thin rectangular nanobar shown in Fig. 2.2(c)].

Because of the non-uniform shape of the rectangular facets (contrast to the uniform circular facets of a cylindrical nanorod), the distribution of charge from the center to the edge of each facet is also non-uniform. In such case, due to the complex nature of the charge distribution, it was not possible to reckon the capacitance and the inductance of a nanobar-like structure by directly applying the expressions of C and L given for the cylindrical nanorod in Eqs. (2.2) and (2.6) above. Hence, it is required to modify the expressions of C and L to make is suitable for the nanobar by playing with the dimension parameters inside Eqs. (2.2) and (2.6). After playing with the dimension parameters l_y and l_z using trial-and-error approach, we found that, if we replace r_0 by $l_z/2$ in Eq. (2.2) and by $l_z/4$ in Eq. (2.3), and rewrite these equations as:

$$C = 2\pi\epsilon_0\epsilon_r\frac{l_z}{2} \qquad [\mathrm{F}] \tag{2.20}$$

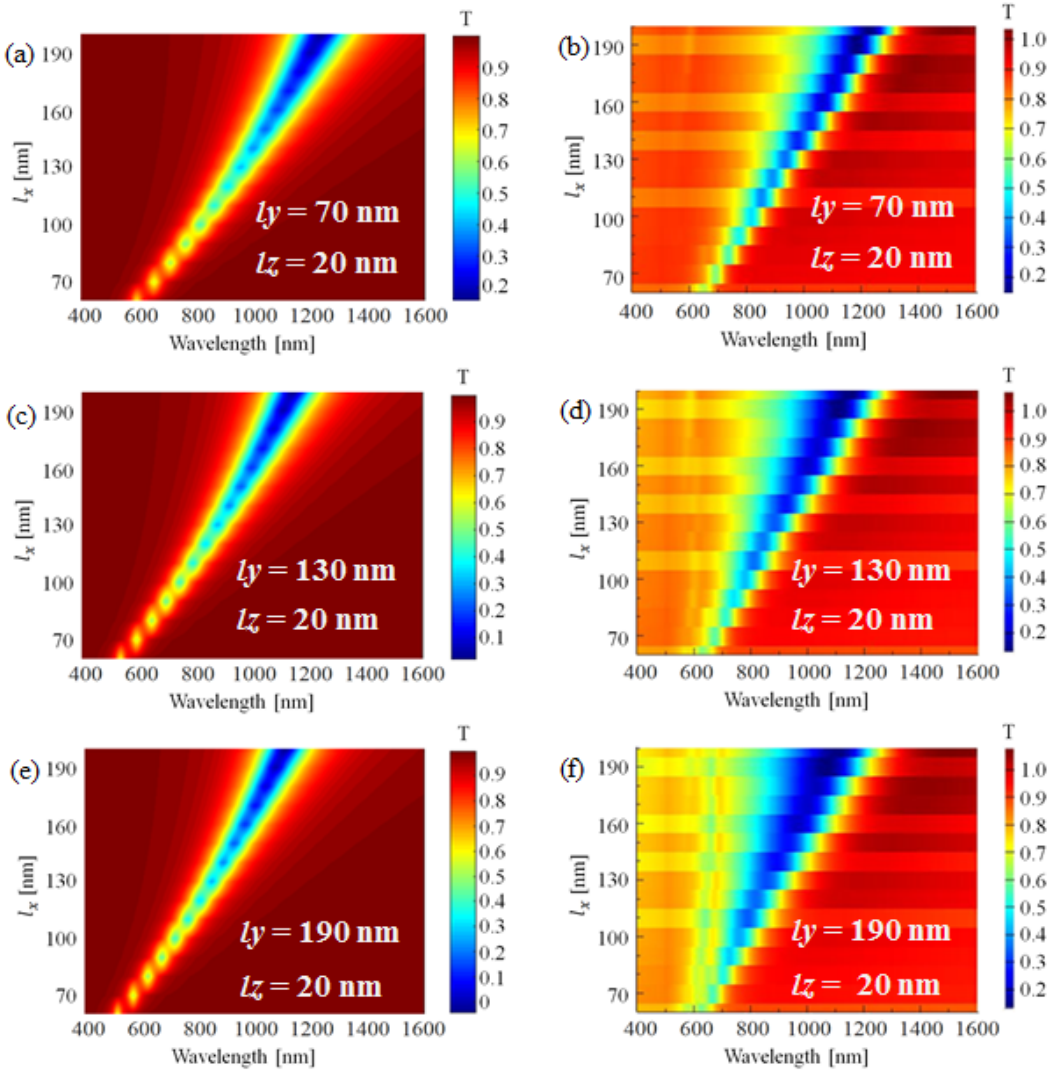

FIGURE 2.5: Comparison between the 2D plots of transmission of a rectangular nanobar as a function of the value of l_x and wavelength, obtained from *RLC* model [(a), (c), (e)] and FDTD simulations [(b), (d), (f)]. In (a) and (b), $l_y = 70$ nm. In (c) and (d), $l_y = 130$ nm, and in (e) and (f), $l_y = 190$ nm. In all the cases [(a)–(f)], $l_z = 20$ nm, and l_x varies from 70 to 200 nm.

and

$$L = L_{\text{self}} + L_{\text{kinetic}} \quad [\text{H}], \tag{2.21a}$$

$$L = \frac{\mu_0 l_x}{2\pi} \log \frac{2l_x}{l_z} + \frac{\mu_0 l_x}{\frac{\omega_p{}^2}{c^2} l_y l_z} \quad [\text{H}]. \tag{2.21b}$$

respectively, the analytically obtained resonant wavelength of the rectangular nanobar agrees well with the simulated value for a range of dimensions, which we are going to discuss now. All the simulations were performed using Lumerical FDTD. In Fig. 2.5, we show the comparison between the *RLC* model and the FDTD simulation for the rectangular nanobar by plotting the transmission as a fuction of two variables: the nanobar's lengths l_x and the corresponding resonant wavelengths λ_0. While in every case l_x was swept from 70 to 200 nm, and l_z was fixed at 20 nm, Figs. 2.5(a-b), (c-d), and (e-f) show the comparison for three different values of l_y: 70 nm, 130 nm, and 190 nm, respectively. It is clear from the graphs that, in the case of a rectangular nanobar, when $l_y = 70$ nm [in Fig. 2.5(a-b)], the *RLC* circuit model provides a good prediction of the resonance position for the swept range of l_x. However, when $l_y = 130$ nm, the *RLC* model only works well for $l_x > 100$ nm [Fig. 2.5(c-d)], and when $l_y = 190$ nm, the *RLC* model only works well for $l_x > 150$ nm [Fig. 2.5(c-d)].

From this observation, we can intuitively conclude that the *RLC* model can only predict the resonant wavelength position with good agreement when the minimum aspect ratio of the length (of a rectangular nanobar) along the polarization direction to the length perpendicular to the polarization direction, $l_x : l_y$, is not less than approximately 5 : 7 (0.7 to 0.75).

If we precisely compare Fig. 2.5(a-b), Fig. 2.5(c-d) and Fig. 2.5(e-f) to each other, contrary to the *RLC* model, we can understand from the FDTD simulation that when the value of l_y increases, for any fixed values of l_x and l_z, the spectral positions of the corresponding resonances become slightly blue-shifted by approximately 100 nm, but only if the aspect ratio $l_x : l_y$ is above 5 : 7. When $l_x : l_y$ is below 5 : 7, the resonant wavelength positions remain almost the same for all the selected values of l_y for any fixed values of l_x and l_z.

Physically or mathematically, it can be better understood from L_{kinetic}, given by Eq. (2.21b). It is clear that if the aspect ratio $l_x : l_y$ becomes lower than 0.5,

then the impact and contribution of the kinetic inductance to the overall inductance becomes less significant. In other words, for these values of $l_x : l_y$, the cloud of the collective electrons will not gain enough kinetic energy from their movement along the light polarization direction to create kinetic inductance.

Another limitation of the proposed *RLC* analytical model, apparent from the side-by-side comparison, is that it still cannot predict the exact linewidth of the resonance shapes (see the graphs for $l_y = 130$ nm and 190 nm). Though it is evident from the FDTD simulation that the linewidths of the resonances get significantly broader with the increase of l_y (especially on the side of the shorter wavelengths from the center wavelength position), as indicated by the increment of the damping constant γ due to the drastic enlargement of the overall nanoparticle size, what lacks is the understanding of how to account for this in *RLC* circuit model.

Nanotriangle, which can be viewed as a nanobar with one end tapered-down, represents a special interest for nonlinear optical experiments due to its low symmetry. Such a triangular nanobar (also called elongated nanoprism) is shown in Fig. 2.2(d); it is a non-centrosymmetric metamolecule and can be utilized for various nonlinear optical processes such as second-harmonic generation (SHG). Therefore, it is instructive to apply *RLC* model described above to a rectangular nanobar in order to describe its resonance characteristics.

We have performed a comparison between the *RLC* model derived for a rectangular nanobar and FDTD simulations performed for triangular elongated nanoprism with the same sweep parameters: l_x in the range between 60 and 200 nm, l_z fixed at 20 nm, and two different values of l_y selected to be 70 and 130 nm [the characteristics corresponding to these two values are depicted in Figs. 2.6(a-b) and (c-d), respectively]. We considered the symmetry axis of our triangular nanoparticle to be aligned with the x-axis (collinear with the polarization orientation), and the corresponding length of the nanoparticle is l_x. In such a way, the triangluar nanobar is oriented in a maximally similar fashion as the rectangular nanobar described earlier. Moreover, l_y is the base of the triangular nanoparticle perpendicular to l_x, which is comparable to l_y of the rectangular bar. The purpose of this comparison is to analyze and understand how well the analytical *RLC* resonator model, derived for the rectangular bar, can describe the elongated nanoprism.

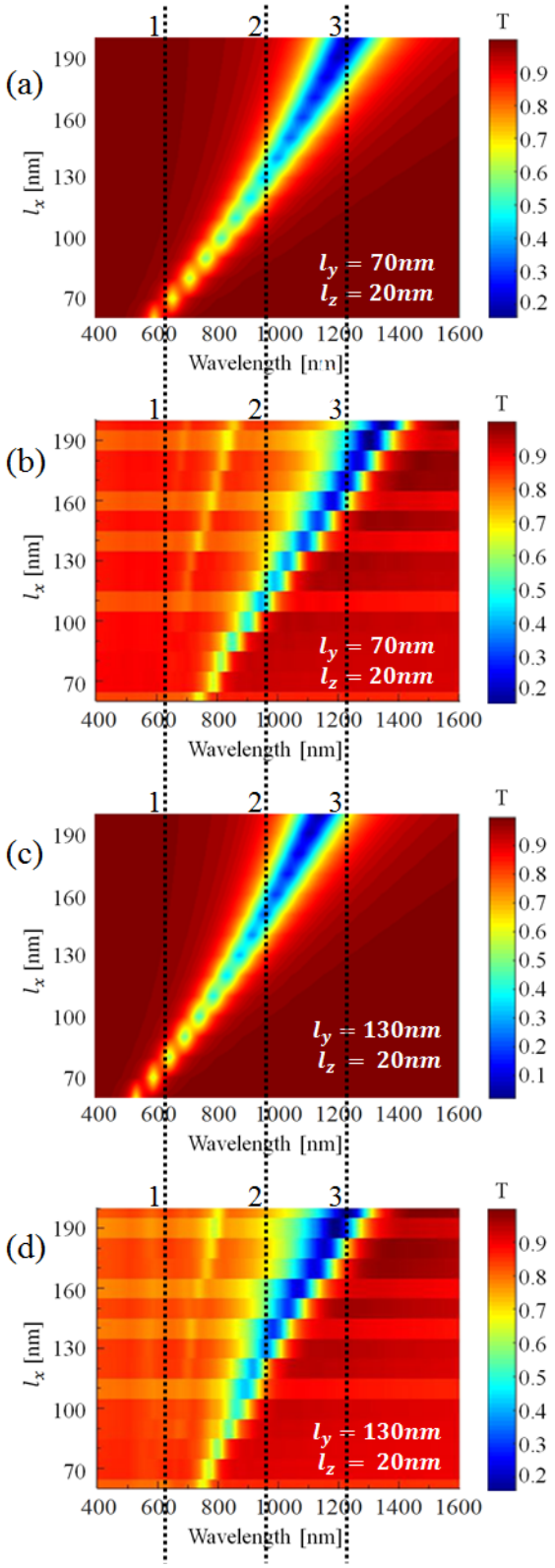

FIGURE 2.6: Comparison between the 2D plots of transmission as a function of the value of l_x and resonant wavelength, obtained from (a) *RLC* model (rectangular bar), (b) FDTD simulation (triangular bar), (c) *RLC* model (rectangular nanobar), and (d) FDTD simulation (triangular nanobar). In (a-b) l_y=70 nm, and (c-d) l_y=130 nm. In all cases (a-d), l_z=20 nm, and l_x varies from 70 nm to 200 nm.

At a first glance, we can observe from Fig. 2.6(a-b) that, when l_y = 70 nm, the simulated resonant wavelengths of the triangular nanobars [shown in Fig. 2.6(b)] are red-shifted by approximately 100 nm compared to the resonant wavelengths of rectangular nanobars with the same l_x [shown in Fig. 2.6(a)]. Note that, a triangular nanoparticle will become an 'elongated' nanoprism (along x-direction) when $l_x > l_y$. Thus, our considered triangular nanoparticle is actually an elongated nanoprism for any value of l_x larger than l_y = 70 nm.

The same is evident from Fig. 2.6(c-d), where the simulated resonant wavelengths in Fig. 2.6(d) for the values of $l_x > l_y$ of the triangular nanoparticle (*i.e.* elongated nanoprism) are red-shifted by approximately 100 nm from the spectral positions of rectangular nanobars with the same values of l_x [shown in Fig. 2.6(c)]. However, for the values of $l_x < l_y$ (when the triangular nanoparticle should no longer be considered as an elongated nanoprism), the redshift of the resonant wavelength positions is approximately 200 nm.

Interestingly, when $l_y = 130$ nm in Fig. 2.6(d), after meeting the condition $l_x > l_y$ to transform the triangular nanoparticle into an elongated nanoprism, the corresponding spectral positions of the resonant wavelength almost matched the wavelength position for the rectangular nanobar with the same values of l_x and l_z but with l_y = 70 nm in Fig. 2.6(a) (which is half of the value of l_y in the case of the elongated nanoprism). To understand more clearly the physics of this phenomenon, let us see the geometrical comparison of both structures, provided in Fig. 2.7.

Let us consider first a rectangular nanobar, shown in Fig. 2.7(a), with the area $A_{\text{rect}} = l_x\, l_{y_{\text{rect}}}$. We introduce the notation $l_{y_{\text{rect}}}$ for the rectangular nanobar's l_y in order to emphasize its distinction from the similar dimension of the nanoprism. In Fig. 2.7(b), we form an isoscales triangle or elongated nanoprism by tapering one end of that rectangular nanobar (the tapered end is on the right-hand side). The dimension of the l_y on the left-hand side remains the same and is equal to $l_{y_{\text{rect}}}$. The area of the triangular elongated nanoprism is $A_{\text{tri}} = \frac{1}{2} l_x\, l_{y_{\text{rect}}}$, which is one half of the area A_{rect} of the rectangular nanobar. This situation corresponds to the red shift in the resonant wavelength of the nanoprism [see Figs. 2.6(a) and (b)].

Let us consider now the situation corresponding to Fig. 2.7(c) where l_y of the elongated nanoprism is twice as large as $l_{y_{\text{rect}}}$. Recall that, to maintain its status as an 'elongated nanoprism', we need to be careful so that l_y cannot be equal or larger than l_x. With this modification of l_y, the overall area A_{tri} of

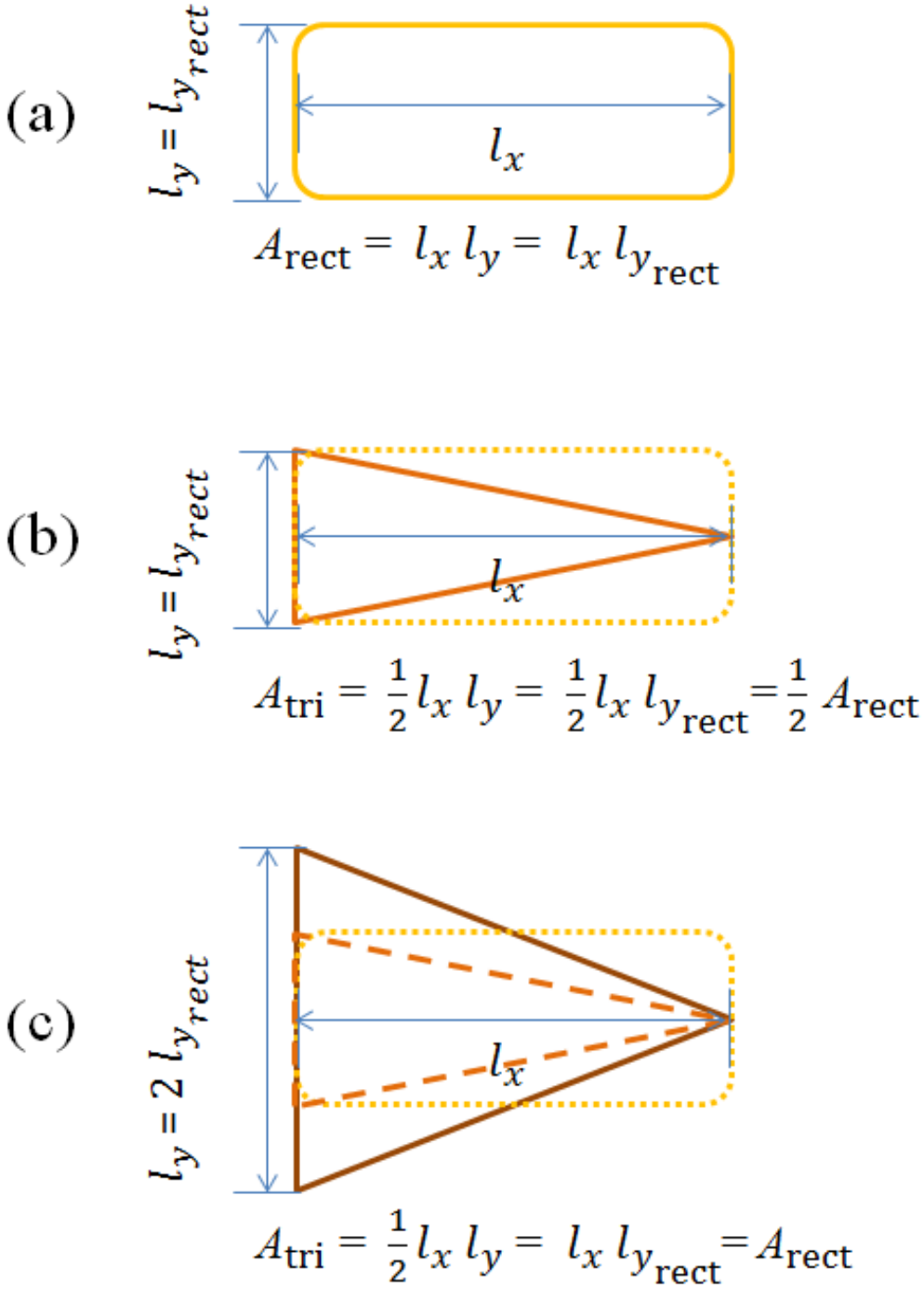

FIGURE 2.7: Schematic of the geometry with dimensions of (a) a rectangular nanobar, (b) an elongated nanoprism formed by tapering one end of the rectangular nanobar, (c) an elongated nanoprism with enlarged dimension of the end opposite to the tapered end.

the elongated nanoprism becomes twice as large and equal to the area A_{rect} of the rectangular nanoparticle shown in Fig. 2.7(a). This makes it clear why the resonant wavelength positions of the elongated nanoprism with $l_y = 130$ nm in Fig. 2.6(d) is almost the same as that of the rectangular nanoparticle with $l_y = 70$ nm, shown in Fig. 2.6(a) (130 nm is numerically almost twice larger than 70 nm).

From this, we can conclude that, with the area increase of the nanoparticle (oriented with its longest dimension collinearly with respect to the incident polarization), the resonant wavelength becomes red-shifted regardless the shape of the nanoparticle. This red shift follows the relationship $\lambda_0 = 2\pi c/\omega_0$ and $\omega_0^2 = 1/LC$, where C and L can be found using Eqs. (2.20) and (2.21b), respectively. On the other hand, if the overall volume and the specific area of the elongated nanoparticle's cross-section perpendicular to the direction of the normally incident light remain the same, no spectral shift of the resonant wavelength should take place.

2.5 Conclusions

In summary, here we demonstrated that the *RLC* model for a simple structure such as cylindrical nanorod can also be implied to determine the linear properties, *e.g.*, linear transmission as a function of the resonant wavelength of other similar and a bit more complex structures, such as rectangular nanobar and elongated triangular nanoprism. Agreement between the results achieved from both the *RLC* model and the numerical FDTD simulation suggests that, when a quick design of any plasmonic structure based on a crude estimate is necessary, using *RLC* circuit model could save one a significant amount of time. This *RLC* circuit model can be utilized not only to design an individual plasmonic metamolecule structure for any particular near-infrared resonant wavelengths, but also to understand the physical origin of the localized surface plasmon resonances (LSPRs) of any plasmonic metamolecule structures.

In Chapter 3, we extend the *RLC* equvalent model of a single elongated nanoprism plasmonic metamolecule to the nonlinear optical regime, and derive its nonlinear polarizability (hyperpolarizability).

Chapter 3

Microscopic nonlinear properties of metamolecules

3.1 Introduction

Plasmonic metamaterials hold promise in many nanophotonics applications such as controlling light in the nanoscale regime, enhancing the localized electromagnetic field near its surface, *etc.* [9]–[11]. Additionally, plasmonic metamaterials can also demonstrate strong nonlinear optical responses, *e.g.*, second-harmonic generation (SHG) and third-harmonic generation (THG) [12], [15], [29], [62], [63].

Like with any other materials, linear and nonlinear properties of plasmonic metamaterial (formed by many metamolecules) are represented by its linear and nonlinear susceptibilities. In the case of individual nanoparticle or metamolecule, the linear and nonlinear properties can be characterized by its linear and nonlinear polarizabilities. Experimentally, the second-order nonlinear polarizability is often measured using incoherent SHG scattering from the nanoparticles known as hyper-Rayleigh Scattering [64]. Therefore, the nonlinear polarizability is also often called hyperpolarizability.

When the fundamental electric field $E(\omega)$ interacts with the nonlinear medium that has the first-, second- and third-order nonlinear polarizabilities (latter two terms are also called first- and second-order hyperpolarizabilities) α, β, and γ, respectively, in the electric-dipole approximation of such light–matter interaction, the resulting linear and nonlinear microscopic polarization or

dipole moments can be written as [62]

$$p^{(1)}(\omega) = \epsilon_0 \, \alpha \, E(\omega) , \tag{3.1a}$$
$$p^{(2)}(\omega) = \epsilon_0 \, \beta \, E(\omega)E(\omega) , \tag{3.1b}$$
$$p^{(3)}(\omega) = \epsilon_0 \, \gamma \, E(\omega)E(\omega)E(\omega) . \tag{3.1c}$$

Now, just for the moment, let us consider a centrosymmetric nonlinear optical material. It is known that an electric field oscillates (alters its direction) repeatedly. This means that, in a centrosymmetric medium, both the linear and nonlinear dipole moments induced by that electric field also change their directions accordingly. Hence, in the equation, the signs of the applied field and the dipole moments change:

$$-p^{(1)}(\omega) = \epsilon_0 \, \alpha \, (-E(\omega)) , \tag{3.2a}$$
$$-p^{(2)}(\omega) = \epsilon_0 \, \beta \, (-E(\omega))(-E(\omega)) , \tag{3.2b}$$
$$-p^{(3)}(\omega) = \epsilon_0 \, \gamma \, (-E(\omega))(-E(\omega))(-E(\omega)) . \tag{3.2c}$$

This yields

$$-p^{(1)}(\omega) = -\epsilon_0 \, \alpha \, E(\omega) , \tag{3.3a}$$
$$-p^{(2)}(\omega) = \epsilon_0 \, \beta \, E(\omega)E(\omega) , \tag{3.3b}$$
$$-p^{(3)}(\omega) = -\epsilon_0 \, \gamma \, E(\omega)E(\omega)E(\omega) . \tag{3.3c}$$

For the first- and third-order linear and nonlinear processes, a comparison between Eqs. (3.3a) and (3.3c) with Eqs. (3.1a) and Eqs. (3.1c) leads to $p^{(1)}(\omega) = p^{(1)}(\omega)$ and $p^{(3)}(\omega) = p^{(3)}(\omega)$, respectively. However, in the case of second-order nonlinearity, a similar comparison of Eqs. (3.3b) and (3.1b) leads to $p^{(2)}(\omega) = -p^{(2)}(\omega)$, which is only possible if $p^{(2)}(\omega) = 0$. It follows from this that the nonlinear polarizability β must vanish in centrosymmetric nanoparticles but not in noncentrosymmetric nanoparticles where the polarization does not simply change its sign following the alternation of the electric field.

Therefore, nonlinear effects and properties are dependent on the material symmetry. While the third-order nonlinear optical processes can take place in all materials, within the electric-dipole approximation of the light-matter interaction, second-order nonlinear optical phenomena, *e.g.*, SHG, can only be allowed in noncentrosymmetric materials [4], [15], [62].

Common plasmonic metals, *e.g.*, gold, silver, copper, or aluminum, wherein

the atoms are organized in a centrosymmetrically-patterned face-centered cubic lattice, have the second-order nonlinear optical processes forbidden in their bulk in the electric dipole approximation [62]. Because of the finite dimension of the atomic lattice at the surface of the metal, the centrosymmetry is locally violated, which allows second-order nonlinear effects to take place only at the surface. However, the surface nonlinear optical signal is typically very weak. In order to observe a considerable second-order nonlinear optical interaction, nanoparticles or metamolecules with noncentrosymmetric shapes are required.

According to hydrodynamic model [62], SHG results only from the motion of the conduction electrons, which is known as the electronic origin of SHG. This concept of the surface electronic contribution towards enhancing nonlinearity is also supported by the time-dependent density function approach. In addition, there also exists a possibility of the contribution to the nonlinear polarizability from the transitions of electrons from d-band to the conduction sp-band. Furthermore, recently it has been revealed that nonlinear quantum tunneling may have an impact on SHG from strongly coupled nanoparticles. From these conceptual facts, there is no question about the significance of the surface contribution to the origin of SHG in plasmonic metal nanoparticles. It is noteworthy to say that, the precise electronic origin of SHG in metals is still under vast and rigorous investigation both theoretically and experimentally [62].

In order to understand the origin of nonlinear effects from individual plasmonic nanoparticles in a simple manner, whether physically or empirically, the nonlinear optical properties of a single nanoparticle due to anharmonic oscillations of its LSPR need to be studied. However, while the nonlinear optical responses of dielectric materials can be easily understood from their linear properties based on anharmonic Lorentz oscillator model of atoms [wherein the electrons are bound to the atom as illustrated in Fig. 3.1(a)], due to the free electrons associated with the surface of plasmonic metal-based nanoparticles, such models cannot be applied to them directly [21], [29]. As a result, one needs to solve the complex Laplace's or Maxwell's equations of the hydrodynamic model or to use nonlinear scattering theory and perform time-consuming numerical simulations such as Finite Element Method (FEM), Finite Difference Time Domain Method (FDTD), *etc.* [28], [29]. But we learned in Chapter 2 that harmonic oscillations associated with LSPRs can be explained well by creating an analogy with equivalent RLC resonator model,

which is formulated to describe the flow of free electrons.

The aim of this chapter is twofold. The first objective is to provide a simple analytical model based on equivalent *RLC* lumped circuit element to derive and understand the electronic origin of the first- and second-order hyperpolarizabilities (second- and third-order nonlinear polarizabilities) of an individual plasmonic metamolecule. Specifically, we studied an elongated nanoprism which lacks center of symmetry with respect to the polarization orientation, as depicted in Fig. 3.1(b-c). We deduce optical nonlinearity from the nanoprism's geometrical parameters, from the information related to the oscillating conduction or free electrons at its surface, and the material properties such as dielectric constant (also called relative permittivity) the of surrounding homogeneous material. The second objective is to extract the value of the first-order hyperpolarizability of individual metamolecules from a 2D plasmonic metasurface using an experimental setup crafted for SHG count measurement. In the previously reported experiment [64], the first-order hyperpolarizability was extracted from hyper-Rayleigh scattering (HRS) of incoherent SHG light scattered from individual plasmonic nanoparticles in an ensemble homogeneous fluid medium. Our technique is the first-ever experimental demonstration of extracting the first-order hyperpolarizability of individual plasmonic metamolecules.

3.2 *RLC* model of nonlinear anharmonic oscillator

Here, we develop a simple and intuitive analytical model that allows one to estimate nonlinear responses of plasmonic metamolecules. The approach is based on an equivalent *RLC* circuit model [65], which is extended to the nonlinear optical regime by introducing a small nonlinear perturbation to the master equation describing the dynamics of the system.

As we saw in Chapter 2, the linear optical response of a metamolecule near its localized surface plasmon resonance (LSPR) can be well understood by forming a crude analog between a driven *RLC* circuit [see Fig. 3.1(c)] and an optical response of the metamolecule. Here we consider an individual plasmonic elongated nanoprism of length l_x [meter (m)], width l_y [m] (of one end) and height or thickness l_z [m].

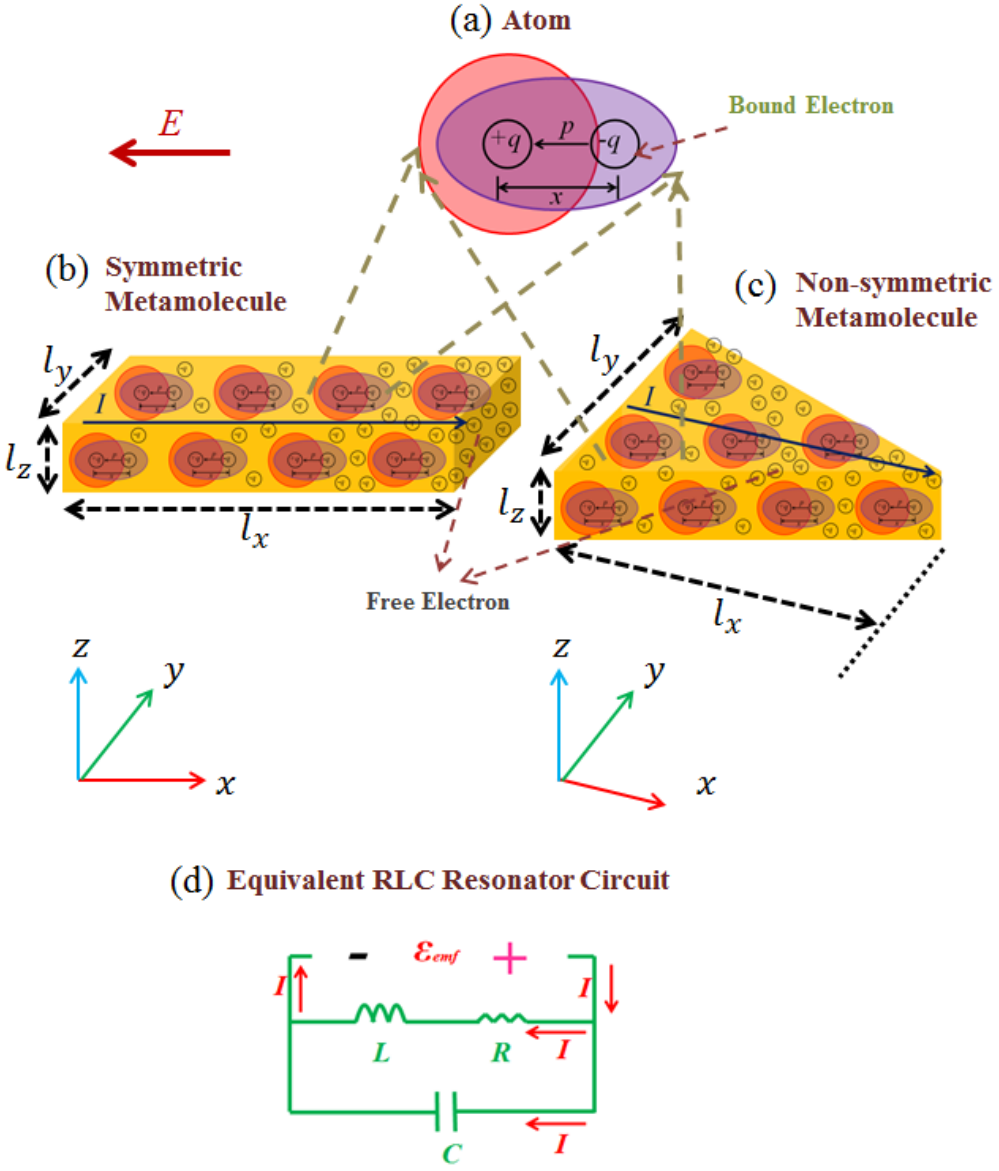

FIGURE 3.1: (a) An atom with a bound electron inside plasmonic metamolecule, (b) a rectangular nanobar representing a centrosymmetric metamolecule, (c) an elongated nanoprism representing a centrosymmetric metamolecule, (d) an equivalent *RLC* circuit diagram.

In the nonlinear optical regime, we can expand the linear charge $\tilde{q}$ in Eq. (2.13) using a procedure analogous to Rayleigh-Schrodinger perturbation expansion [4], [65]:

$$\Longrightarrow \qquad \ddot{\tilde{q}} + 2\gamma\dot{\tilde{q}} + \omega_0^2\tilde{q} + a\omega_0^2\tilde{q}^2 - b\omega_0^2\tilde{q}^3 = -C\lambda\omega_0^2 l_x \tilde{E}_{\text{inc}} \qquad \left[\frac{\text{Coul}}{\text{s}^2}\right]. \tag{3.4}$$

Here λ is the strength of the perturbation, and a and b are second- and third-order nonlinear coefficients. The solution to Eq. (3.4) can be written in the form of a power series expansion with respect to λ:

$$\tilde{q} = \lambda\tilde{q}^{(1)} + \lambda^2\tilde{q}^{(2)} + \lambda^3\tilde{q}^{(3)} + ... \qquad [\text{Coul}]\,. \tag{3.5}$$

In the linear case, for both the nanobar and the elongated nanoprism, the term λ leads to the equation:

$$\ddot{\tilde{q}}^{(1)} + 2\gamma\dot{\tilde{q}}^{(1)} + \omega_0^2\tilde{q}^{(1)} = -C\omega_0^2 l_x \tilde{E}_{\text{inc}} \qquad [\text{Coul}]\,, \tag{3.6}$$

Here, we treat the nonlinear optical effects that occur without change in the frequency spectrum. We assume that the incident electric field is monochromatic with the fundamental frequency ω:

$$\tilde{E}_{\text{inc}}(t) = E_{\text{inc}}\exp(-i\omega t) + \text{c. c.} \qquad [\text{Coul}]\,. \tag{3.7}$$

Hence, Eq. (3.6) has a steady-state solution:

$$\tilde{q}^{(1)}(t) = q^{(1)}(\omega)\exp(-i\omega t) + \text{c. c.} \qquad [\text{Coul}]\,. \tag{3.8}$$

Here the amplitude $q(\omega)$ has the form:

$$q^{(1)}(\omega) = -\frac{C\omega_0^2 l_x E_{\text{inc}}(\omega)}{D(\omega)} \qquad [\text{Coul}]\,, \tag{3.9}$$

where $D(\omega) = \omega_0^2 - 2i\gamma\omega - \omega^2$ is a complex denominator function related to the localized surface plasmon resonance frequency ω_0. However, the terms λ^2 and λ^3 lead to separate equations for the second- and third-order contributions (for either the nanobar or the elongated prism). In the case of the nanobar, the second-order contribution is governed by the equation:

$$\ddot{\tilde{q}}^{(2)} + 2\gamma\dot{\tilde{q}}^{(2)} + \omega_0^2\tilde{q}^{(2)} = 0\,. \tag{3.10}$$

Note that there is no term in Eq. (3.10) containing the nonlinear strength coefficient a as $\chi^{(2)} = 0$. Since Eq. (3.10) is damped but not driven, its steady-state solution vanishes, resulting in:

$$\tilde{q}^{(2)} = 0\,. \tag{3.11}$$

On the other hand, for the elongated prism, the second-order contribution can be expressed in the following form:

$$\ddot{\tilde{q}}^{(2)} + 2\gamma\dot{\tilde{q}}^{(2)} + \omega_0^2\tilde{q}^{(2)} + a\omega_0^2[\tilde{q}^{(1)}(\omega)]^2 = 0\,. \tag{3.12}$$

After substituting the expression for $\tilde{q}^{(1)}$ given by Eq. (3.9) into Eq. (3.12), we can re-write it as:

$$\ddot{\tilde{q}}^{(2)} + 2\gamma\dot{\tilde{q}}^{(2)} + \omega_0^2\tilde{q}^{(2)} = -a\omega_0^2\left[\frac{C\omega_0^2 l_x E_{\text{inc}}(\omega)}{D(\omega)}\right]^2 \qquad [\text{Coul}]\,. \tag{3.13}$$

This equation has a steady-state solution:

$$\tilde{q}^{(2)} = q^{(2)}(2\omega)\exp(-2i\omega t) \qquad [\text{Coul}]\,. \tag{3.14}$$

Eqs. (3.14) and (3.9) into Eq. (3.13) yields:

$$q^{(2)}(2\omega) = \frac{-aC^2{\omega_0}^6 l_x^2 E_{\text{inc}}^2(\omega)}{D^2(\omega)D(2\omega)} \qquad [\text{Coul}]\,, \tag{3.15}$$

where $D(2\omega) = (\omega_0^2 - 4i\gamma\omega - (2\omega)^2)$ is the complex denominator function related to the second-harmonic signal corresponding to the fundamental localized surface plasmon resonance frequency ω_0.

In the case of the third-order contribution, for both the nanobar and the elongated nanoprism, λ^3 leads to the equation:

$$\ddot{\tilde{q}}^{(3)} + 2\gamma\dot{\tilde{q}}^{(3)} + \omega_0^2\tilde{q}^{(3)} - b{\omega_0}^2[\tilde{q}^{(1)}(\omega)]^3 = 0\,, \tag{3.16}$$

After substituting the expression for $\tilde{q}^{(1)}$ given by Eq. (3.9) into Eq. (3.16), we can re-write it as:

$$\ddot{\tilde{q}}^{(3)} + 2\gamma\dot{\tilde{q}}^{(3)} + \omega_0^2\tilde{q}^{(3)} = b{\omega_0}^2\left[-\frac{C\omega_0^2 l_x E_{\text{inc}}(\omega)}{D(\omega)}\right]^3 \qquad [\text{Coul}]\,. \tag{3.17}$$

This equation has a steady-state solution in the form:

$$\tilde{q}^{(3)} = q^{(3)}(3\omega)\exp(-3i\omega t) \qquad [\text{Coul}]\,, \tag{3.18}$$

Substituting Eqs. (3.18) and (3.9) into Eq. (3.17) leads to the equation:

$$q^{(3)}(3\omega) = \frac{-bC^3{\omega_0}^8 l_x^3 E_{\text{inc}}^3(\omega)}{D^3(\omega)D(3\omega)} \qquad [\text{Coul}]\,, \tag{3.19}$$

where $D(3\omega) = (\omega_0^2 - 6i\gamma\omega - (3\omega)^2)$ is a complex denominator function related to the third-harmonic (THG) signal corresponding to the fundamental localized surface plasmon resonance frequency ω_0.

Now we are all set to derive linear and nonlinear polarizabilities. From the definition of the induced dipole moment $p(\omega')$, we can relate it to the charge $q(\omega')$ as:

$$p^{(1)}(\omega) = q^{(1)}(\omega)\ l_x \qquad [\text{Coul.m}]\,, \tag{3.20a}$$
$$p^{(2)}(2\omega) = q^{(2)}(2\omega)\ l_x \qquad [\text{Coul.m}]\,, \tag{3.20b}$$
$$p^{(3)}(3\omega) = q^{(3)}(3\omega)\ l_x \qquad [\text{Coul.m}]\,. \tag{3.20c}$$

The total induced dipole moment p can be defined as:

$$p(\omega') = p^{(1)}(\omega) + p^{(2)}(2\omega) + p^{(3)}(3\omega) + ... \qquad [\text{Coul.m}]\,, \tag{3.21}$$

where the various terms can be expressed as:

$$p^{(1)}(\omega) = \epsilon_0\alpha(\omega;\omega)E_{\text{inc}}(\omega) \qquad [\text{Coul.m}]\,, \tag{3.22a}$$
$$p^{(2)}(2\omega) = \epsilon_0\beta(2\omega;\omega,\omega)E_{\text{inc}}^2(\omega) \qquad [\text{Coul.m}]\,, \tag{3.22b}$$
$$p^{(3)}(3\omega) = \epsilon_0\gamma(3\omega;\omega,\omega,\omega)E_{\text{inc}}^3(\omega) \qquad [\text{Coul.m}]\,. \tag{3.22c}$$

where $\epsilon_0 = 8.85 \times 10^{-12}$ [F m^{-1}] is the vacuum permittivity, and α, β and γ are the linear polarizability, and first-order and second-order hyperpolarizabilities, respectively.

Substituting Eqs. (3.9), (3.22b) and (3.22c) into Eqs. (3.20a), (3.20b) and (3.20c), respectively, we can obtain the expressions for the linear polarizability and

nonlinear hyperpolarizabilities as follows:

$$\alpha(\omega) = -\frac{C{\omega_0}^2{l_x}^2}{\epsilon_0 D(\omega)} \quad [\mathrm{m}^3], \tag{3.23a}$$

$$\beta(2\omega;\omega) = -a\frac{C^2{\omega_0}^6{l_x}^3}{\epsilon_0 D(2\omega)D^2(\omega)} \quad [\frac{\mathrm{m}^4}{\mathrm{V}}], \tag{3.23b}$$

$$\gamma(3\omega;\omega) = -b\frac{C^3{\omega_0}^8{l_x}^4}{\epsilon_0 D(3\omega)D^3(\omega)} \quad [\frac{\mathrm{m}^5}{\mathrm{V}^2}]. \tag{3.23c}$$

Here the nonlinear coefficients a and b are still unknown. Now we will focus on extracting the numerical values of a and b.

3.2.1 Nonlinear coefficients and hyperpolarizabilities

In Eqs. (3.23b) and (3.23c), the values of every parameter on the right-hand side are known, except for those of the nonlinear strength coefficients a and b. If we calculate the units of all parameters except a and b off-resonance (when the nonlinear denominators D are undamped), we find that the unit of the term on the right-hand side of Eq. (3.23b) becomes Fm^4 , and in case of Eq. (3.23c), the units become $\mathrm{F}^2\mathrm{m}^5$. To match the units of the right-hand sides to those of the left-hand sides, the units of a and b must be $\mathrm{F}^{-1}\ \mathrm{V}^{-1}$ and $\mathrm{F}^{-2}\ \mathrm{V}^{-2}$, respectively. We can also validate this fact by the restoring force relationship given by Eq. (3.4):

$$\tilde{q} + a\tilde{q}^2 = 0 \quad [\mathrm{Coul}] \quad \text{or} \quad [\mathrm{FV}], \tag{3.24a}$$

$$\Longrightarrow \quad a = -\frac{1}{\tilde{q}} \quad [\frac{1}{\mathrm{Coul}}] \quad \text{or} \quad [\frac{1}{\mathrm{FV}}], \tag{3.24b}$$

and

$$\tilde{q} - b\tilde{q}^3 = 0 \quad [\mathrm{Coul}] \quad \text{or} \quad [\mathrm{FV}], \tag{3.25a}$$

$$\Longrightarrow \quad b = \frac{1}{\tilde{q}^2} \quad [\frac{1}{\mathrm{Coul}^2}] \quad \text{or} \quad \left[\frac{1}{\mathrm{F}^2\mathrm{V}^2}\right]. \tag{3.25b}$$

As we know, $\tilde{q} = CV$, where the unit of the capacitance C is F and the unit of the voltage V is V. We can write from Eqs. (3.24b) and (3.25b):

$$a = -\frac{1}{CV} \quad \left[\frac{1}{\mathrm{FV}}\right]. \tag{3.26}$$

and

$$b = -\frac{1}{C^2V^2} \quad \left[\frac{1}{\mathrm{F}^2\mathrm{V}^2}\right]. \tag{3.27}$$

Here, the details of the voltage V are missing. In this case, if we recall the energy, E [J] - voltage, V [V] relationship, we can write:

$$V = \frac{E}{e} \quad [\frac{\mathrm{J}}{\mathrm{Coul}}], \tag{3.28}$$

where $e = 1.6 \times 10^{-19}$ Coul is the elementary charge of an electron. We can also re-write Eq. (3.28) using Planck's equation:

$$V = \frac{h\nu_{\mathrm{SHG,\,THG}}}{e} \quad [\frac{\mathrm{eV}}{\mathrm{Coul}}], \tag{3.29a}$$

$$\implies \quad V = \frac{hc}{e\lambda_{\mathrm{SHG,\,THG}}} \quad [\frac{\mathrm{eV}}{\mathrm{Coul}}]. \tag{3.29b}$$

Substituting Eq. (3.29b) into Eqs. (3.26) and (3.27), we obtain the expressions:

$$a = -\frac{1}{C}\frac{e\lambda_{SHG}}{hc} \quad [\frac{1}{\mathrm{FV}}] \tag{3.30}$$

and

$$b = -\frac{1}{C^2}\frac{e^2\lambda_{THG}^2}{h^2c^2} \quad [\frac{1}{\mathrm{F}^2\mathrm{V}^2}] \tag{3.31}$$

for the nonlinear coefficients a and b. We provided these expressions in terms of the second-and third-harmonic wavelengths λ_{SHG} and λ_{THG} because as the next step we compare the analytical result for second-order nonlinear optical response (first-order hyperpolarizability) with SHG experimental data. We plan to do the comparison for the second-order hyperpolarizability in the future.

Substituting Eq. (3.30) for the nonlinear coefficient a and Eq. (2.20) for the capacitance C into Eq. (3.23b), we find the expression for the first nonlinear hyperpolarizability in terms of known parameters:

$$\implies \quad \beta(2\omega;\omega) = -\frac{-e\lambda_{SHG}}{hc}\frac{\pi\epsilon_r {l_x}^3 l_z {\omega_0}^6}{D(2\omega)D^2(\omega)} \quad [\frac{\mathrm{m}^4}{\mathrm{V}}]. \tag{3.32a}$$

Similarly, substituting Eq. (3.31) for b and Eq. (2.20) for C into Eq. (3.23c) results in the expression:

$$\implies \quad \gamma(3\omega;\omega) = -\frac{-e^2\lambda_{THG}^2}{h^2c^2}\frac{\pi\epsilon_r {l_x}^4 l_z {\omega_0}^8}{D(3\omega)D^3(\omega)} \quad [\frac{\mathrm{m}^5}{\mathrm{V}^2}] \tag{3.33a}$$

for the second nonlinear hyperpolarizability. Under off-resonance conditions, Eqs. (3.32a) and (3.33a) can be re-written as:

$$\beta = -{l_x}^3 l_z \frac{-\pi\epsilon_r e\lambda_{SHG}}{hc} \qquad [\frac{\mathrm{m}^4}{\mathrm{V}}], \tag{3.34}$$

and

$$\gamma = -{l_x}^4 l_z \frac{-\pi\epsilon_r e^2\lambda_{THG}^2}{h^2c^2} \qquad [\frac{\mathrm{m}^5}{\mathrm{V}^2}]. \tag{3.35}$$

Next, we plug the numerical values of all the parameters into Eq. (3.34). The values for the geometrical dimensions are provided in Chapter 2). We consider $\lambda_0 = 1100$ nm for the fundamental wavelength, and $\lambda_{SHG} = 550$ nm and $\lambda_{THG} = 366.67$ nm for the second and third harmonics, respectively. This results in the following values of the hyperpolarizabilities β and γ:

$$\beta = -(157\times10^{-9})^3 \times 20\times10^{-9} \times \frac{3.14\times3.9\times-(-1.6\times10^{-19})\times550\times10^{-9}}{6.63\times10^{-34}\times3\times10^8}$$

$$= -8.39\times10^{-28} \quad [\frac{\mathrm{m}^4}{\mathrm{V}}], \tag{3.36}$$

and

$$\gamma = -(157\times10^{-9})^4 \times 20\times10^{-9} \times \frac{3.14\times3.9\times-(-1.6\times10^{-19})^2\times(550\times10^{-9})^2}{(6.63\times10^{-34})^2\times(3\times10^8)^2}$$

$$= 2.9\times10^{-35} \qquad [\frac{\mathrm{m}^5}{\mathrm{V}^2}]. \tag{3.37}$$

If we compare the order-of-magnitude estimate of the first- and second-order hyperpolarizabilities β and γ that we performed using RLC model with the value extracted experimentally by hyper-Rayleigh-scattering in [64], [66], we can see a nice agreement between them.

3.3 Comparison with the experimental data

As a part of this Master's thesis effort, we conducted an experiment on measuring the first nonlinear hyperpolarizability (the second-order susceptibility

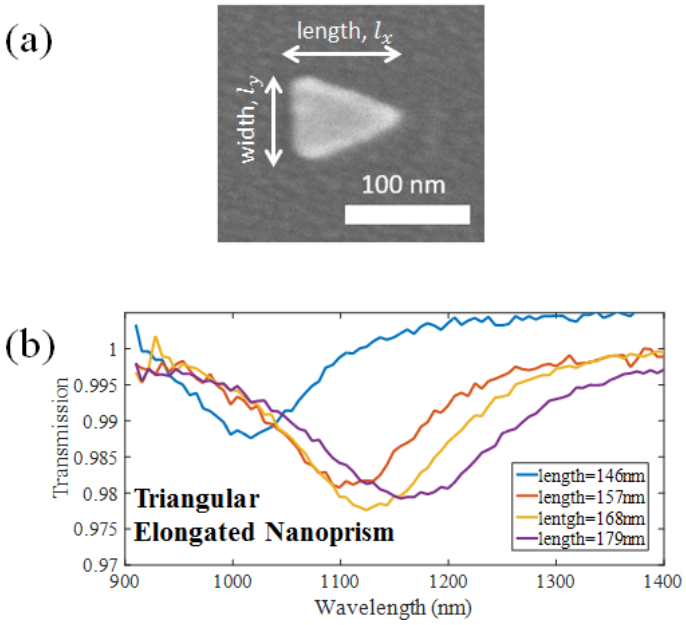

FIGURE 3.2: (a) SEM image of an individual elongated nanoprism. (b) Measured transmission spectra of the LSPRs of the elongated nanoprisms with four different lengths along the polarization direction.

per one metamolecule) of an elongated nanoprism. Technically, such measurement implies detecting the nonlinear optical signal from a single isolated metamolecule, which is extremely challenging as such signal is very weak. For the reason, we rather consider an irregular array of such nanoprisms oriented in the same direction. The irregularity in the nanoprisms placement ensures the elimination of any lattice resonant effects (there are undesired in the situation when a single nanoprism's optical response is assessed) [9], [16], [41]. Effectively, such a nanoprism can be considered as embedded in a homogeneous background with the refractive index n. We performed the experiment using the same fabricated sample as that used for the linear optical experiment described in Chapter 2. This choice of the metamolecules (the elongated nanoprisms embedded in a homogeneous medium was made because they lack axial symmetry: noncentrosymmetric shapes exhibit enhanced second-order nonlinear optical response [12]. Also, due to the close similarity of the geometries, the equivalent *RLC* circuit for this type of structure can be easily redefined by slight modification to the model available for cylindrical nanorods (see Chapter 2 for the details).

The experiment was performed jointly by our collaborator Dr. Mikko Huttunen (from Prof. Martti Kauranen's Nonlinear Optics group at the Tampere University in Finland) and me in the Photonics Laboratory at the Tampere

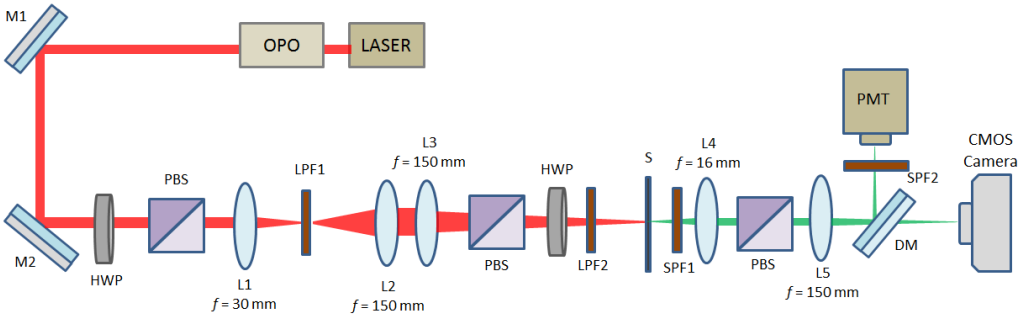

FIGURE 3.3: Schematic representation of the experimental setup for measuring SHG. M – mirrors, HWP – motorized half-wave plates, P – polarizers, S - sample, L – lenses (L1 has $f = 30$ mm, L2 has $f = 150$ mm, L3 has f=150 mm, L4 has f=16 mm, L5 has f=150 mm, L1, L2, L3, and L5 – achromats). LPF — long-pass filter at 900 nm, SPF1 — short-pass filter at 700 nm, A – film polarizer (analyzer), DM – dichroic mirror, SPF2 – short-pass filter at 900 nm, PMT – photomultiplier tube (PicoQuant PMA-C 192-M).

University. To experimentally observe the SHG, an incident fundamental pulsed laser beam (Chameleon Vision II, Ti:Sapphire) with the repetition rate $R = 82$ MHz, pump wavelength $\lambda_{\text{fund}} = 770$ nm was combined with an optical parametric oscillator's beam (OPO, Chameleon Compact with the scanning wavelength range from 1000 to 1300 nm, pulse length $\tau_p = 200$ fs) and was focused onto the randomized array of metamolecules in normal direction with the polarization aligned along the length l_x of the metamolecules (along the x-axis). The input pulsed laser power P_ω was 8 mW. The SHG light was detected in transmission using a photomultiplier tube (PMT) module. The details of the setup were also given for another similar experiment in ref. [53].

A schematic of the SHG experimental setup is illustrated in Fig. 3.3. A motorized achromatic half-wave plate (HWP) and a polarizer were used to control the level of power P_ω from the OPO. Before entering the polarization-control part of the setup, the fundamental beam was cleaned and expanded with a set of lenses and an aperture (diameter $D = 25$ μm). To weakly focus the beam on the sample arrays, an achromatic lens with the focal length of 150 mm was used, ensuring a relatively small beam waist diameter of the excitation beam (around 100 μm) while the plane-wave approximation could still be used. To control the input polarization, we used a high-quality polarizer and an achromatic HWP, whereas to select the polarization of the emitted SHG light, we used a film polarizer after the sample. Then, to pass (block)

the fundamental beam, we used a 900 nm long-pass (700 nm short-pass) filter. To efficiently collect the generated SH signal, a lens with the focal length of 16 mm was used after the sample. After being reflected by a dichroic mirror and passing through another short-pass filter (900 nm), the SHG signal was focused on the active area of a photomultiplier tube (PMT) module with another achromatic lens of 150 mm focal length. For sample alignment, the light transmitted through the dichroic mirror was used to image the sample plane with a CMOS camera and a camera lens (MVL50M23).

The PMT has been calibrated using a sensitive power meter, and the result is that 1 count/s corresponds to 5.2 aW. Fig. 3.4(a) shows the measured SHG power spectra as the function of the OPO wavelength for four different arrays of the randomly arranged elongated nanoprism metamolecules with lengths $l_x = 146$ nm, 157 nm, 168 nm and 179 nm. It is clear from Fig. 3.4(b) that the typical value of the output SHG power is a few fW.

We now retrieve the first-order hyperpolarizability β using the obtained SHG power following the equation which is given below [67]:

$$P_{2\omega}^{(x\to x)} = \frac{16\pi^3 \ln 2}{cR\tau_p}\sqrt{\frac{2\ln 2}{\pi}}\frac{[t_{af}^{(1x)}]^4[t_{fs}^{(2x)}]^2[t_{sa}^{(2x)}]^2}{n_2^2}\frac{P_\omega^2}{A}\left(\frac{2\pi L}{\lambda_{\text{fund}}}\right)^2\chi_{xxx}^2\frac{\sin^2\psi}{\psi^2}\,, \quad (3.38)$$

where t_{af}, t_{fs}, t_{sa} are the Fresnel transmission coefficients at the interference between different media air a, film (or top layer), f, substrate s.

Now, we know that, for any interface between two media 1 and 2, the Fresnel coefficient is:

$$t_{12} = \frac{2n_1\cos\theta_1}{n_2\cos\theta_1 + n_1\cos\theta_2}\,. \quad (3.39)$$

For normal incidence of light, $\theta_1 = \theta_2 = 0$; henceforth t_{12}=1. Since we are shining the sample by the laser beam from the normal direction, in Eq. (3.38), we can also consider that $t_{af} = t_{fs} = t_{sa} = 1$. Also,

$$\psi = \frac{2\pi L}{\lambda_{\text{fund}}}(n_1c_1 - n_2c_2)\,, \quad (3.40)$$

where

$$c_m = \sqrt{1 - \left(\frac{1}{n_m}\right)^2\sin^2\theta}\,, \quad (3.41)$$

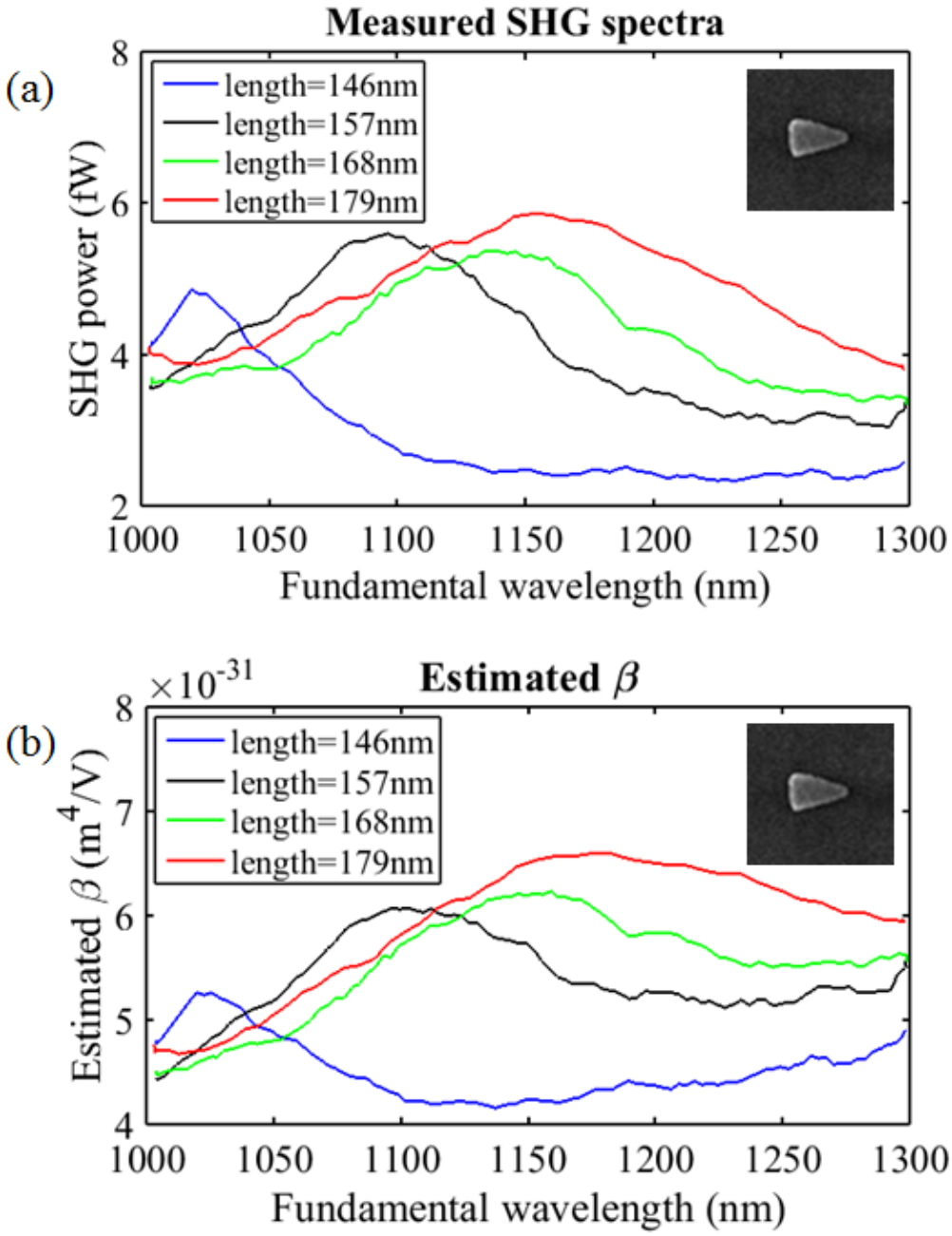

FIGURE 3.4: (a) Measured SHG output power from the random array of metamolecules detected by PMT, (b) estimated first-order hyperpolarizability β. (Inset: SEM image of an elongated nanoprism.

and $m = 1, 2, ...$ The light velocity in vacuum $c = 3 \times 10^8$ m/s, n_1=1 and n_2=1.46. Note that, beam focus area $A=\pi(D/2)^2$. The remaining two unknown parameters in Eq. (3.38) are L (the thickness of the individual metamolecules l_z) and the second-order susceptibility $\chi_{xxx}=\chi^{(2)}$ of the whole array. By considering $L = l_z = 20$ nm, and taking the value of $P_{2\omega}$ on the left-hand-side of Eq. (3.38) to be the same as its value obtained in experiment for the particular fundamental wavelength of incident laser beam, we can obtain the order-of-magnitude estimate for the second-order nonlinear susceptibility $\chi^{(2)} = 10^{-12}$ m/V. Let us recall now that the nonlinear susceptibility can be expressed in terms of its microscopic counterpart, the nonlinear hyperpolarizability, and the molecular or atomic density as

$$\chi^{(2)} = N\beta\,. \tag{3.42}$$

Here N represents the number of metamolecules per effective volume of the array and can be calculated to be $N = 5 \times 10^{19}$ m^{-3} from the effective volume of the array 200 μm $\times$ 200 μm $\times$ 20 nm $= 8 \times 10^{-16}$ m^3 and the total number of metamolecules randomly arranged in the array $200 \times 200 = 40,000$. We can now estimate the order-of-magnitude value of the first-order hyperpolarizability $\beta = 10^{-31}$ m^4/V [shown in fig. 3.4(b)].

It appears that the measured value of β is two or three orders of magnitude lower compared to its value obtained from the analytical model. One possible solution of this discrepancy might be in considering the number of the metamolecules only in y-direction, which is orthogonal to the direction of the light polarization. Thus, we can assume that the number of the metamolecules is only 200, which results in the estimated density $N = 2.5 \times 10^{17}$ m^{-3}. Then the order-of-magnitude value of β becomes 10^{-29} m^4/V, which is close to the value 10^{-28} m^4/V, obtained analytically.

3.4 Conclusions

In this chapter, we demonstrated that, similar to a dielectric atomic system, nonlinear properties of individual plasmonic metamolecules can also be estimated. The difference between the two cases is as follows. In case of a dielectric material, we consider each atom as an equivalent mass-spring mechanical oscillator, while in case of plasmonic metamolecules, we recall the equivalent RLC electrical lumped circuit model for individual metamolecules.

We demonstrated, by the pen and paper calculation, that the order-of-magnitude estimate of the first- and second-order hyperpolarizabilities β and γ of an asymmetrically shaped metamolecule such as an elongated nanoprism can be obtained without resorting to computation-intensive numerical methods. The theoretically estimated values agree with the previously reported experimental values obtained from the hyper-Rayleigh scattering from the ensemble cylindrical gold nanoparticles in the fluid [56], [64], [66].

In order to further validate our model, we conducted an experiment of our own using a different approach compared to that reported in [64]. We experimentally measured SHG signal from an irregular array of elongated nanoprisms and estimated the value of the first-order hyperpolarizability β. The experimentally extracted data slightly disagreed with the order-of-magnitude of the analytical value of β. One thing we realized is, we did not know the impact of the density N of the metamolecules on the overall SHG response and the overall second-order susceptibility $\chi^{(2)}$. Thus, we cannot draw conclusions just based on the current experimental result. In future, we plan to fabricate more samples with different density N of the metamolecules in different 2D metasurface arrays.

In the following chapter 4, we switch the gears and present a different research project falling within the research plan of the present Master's thesis work, which is hybrid plasmonic Fabry-Perot cavity resonances.

Chapter 4

Surface lattice and hybrid plasmonic-cavity resonances

4.1 Introduction

Localized surface plasmon resonances (LSPRs) arising from individual plasmonic nanoparticles can greatly enhance the optical field confinement within a subwavelength region. This enhanced field could enable strong light-nanoparticle interactions. However, the strong field confinement associated with the metamolecules is often accompanied with very high absorption loss, which hinders many potential applications.

Plasmonic nanoparticles are frequently referred to as metamolecules since they act as the core-blocks of any plasmonic metamaterials, *e.g.*, 2D metasurfaces [9]. When many plasmonic metamolecules are arranged in a periodic lattice with a periodicity P in a homogeneous dielectric medium of refractive index n, the LSPRs that arise from individual metamolecules can couple to in-plane diffraction orders (DOs) of the array to generate new hybrid resonances known as surface lattice resonances (SLRs) [16], [30]. The linewidth of such SLRs is typically much narrower than their largely broad LSPR counterpart, resulting in much higher quality factor or Q-factor which could enable many realistic implementations in nonlinear optics necessitating low loss [41], [53], [55], [56].

This narrowband high-Q SLR mode typically appears far from the main center wavelength of the LSPR. For high-intensity applications such as nonlinear SHG, SLRs are the good choice, since one can increase the intensity of the incident laser without worrying about damaging the metal nanoparticles on the resonant frequency. However, for some other nonlinear applications

such as three- and four-wave-mixing processes, THz generation, cascaded nonlinear process, *etc*. one needs to excite the material by another low power light source with a different wavelength. In such a case, generating other, additional narrowband high-Q modes is of high importance. Thanks to the enhancement of the local field, LSPR itself facilitates any nonlinear process. Keeping this fact in mind, generating high-Q modes on LSPR lineshape could be a great advantage for any nonlinear process in plasmonic metasurface.

In ref. [57], Schmidt, *et al.* demonstrated that when a plasmonic nanoparticle is placed on a high-index microresonator cavity (here the cavity is formed by a thin film of high index material with micrometer thickness), the LSPR corresponding to the nanoparticle is modified through hybridization with the characteristic Fabry-Perot resonance of that microcavity. The modified broad LSPR will then be divided into multiple discrete narrowband hybrid modes with different intensity levels, where the most intense narrowband hybrid resonance will appear on or near the center wavelength of the original LSPR lineshape.

Here, we show that a 2D-metasurface with periodically arranged metamolecules can, in fact, combine the hybrid plasmonic-cavity resonances with SLR simply by selecting the proper periodicity of the lattice and the thickness of the top-cladding layer t_{top}.

4.2 Combination of hybrid plasmonic-cavity resonances with SLR

First, we designed a plasmonic metasurface to observe SLR around 1550 nm optical telecommunication wavelength. Fig. 4.1 shows the schematic of the designed plasmonic metasurface. The plasmonic metasurface is comprised of rectangular arrays of gold metamolecules with 2D periodicity of $P_x = 500$ nm and $P_y = 1062$ nm in the xy plane (the plane of the metasurface). The dimensions of the individual metamolecules are $l_x = 200$ nm, $l_y = 130$ nm, and $l_z = 20$ nm, and the light is incident along the z-direction. Based on the interaction of the metamolecules in y-direction, the SLR should arise near the Rayleigh Anomaly (RA) wavelengths that can be determined from the

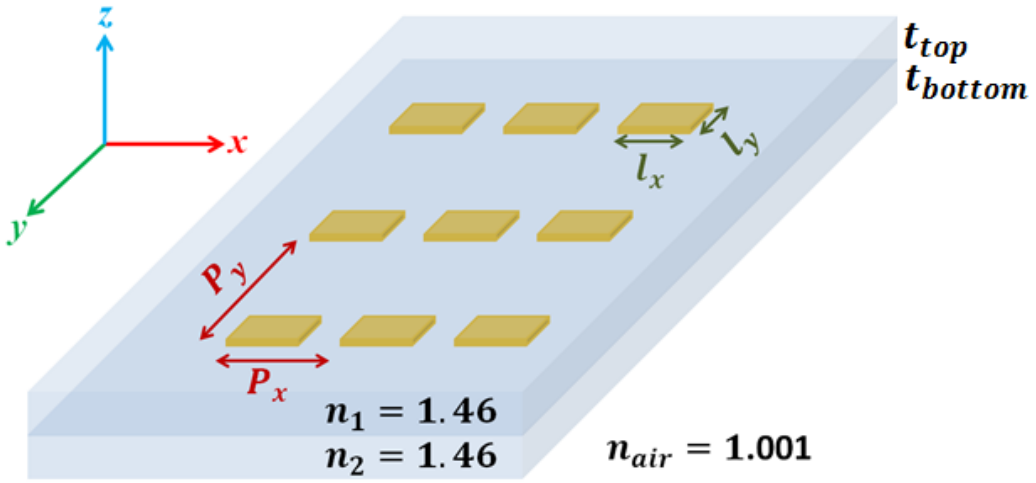

FIGURE 4.1: Schematic of the periodic array of the 2D plasmonic metasurface for LSPR and SLR observation.

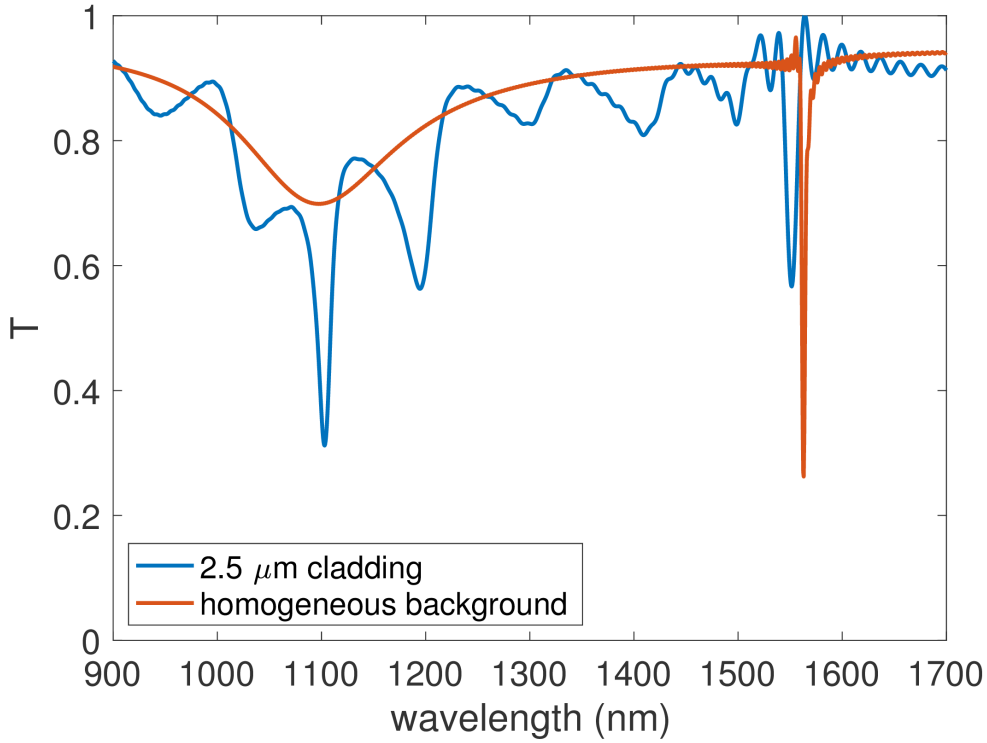

FIGURE 4.2: FDTD simulation comparing the transmission spectra of a metasurface with $t_{\text{top}} = 2.5$ μm thick cladding and infinitely thick cladding (very thick homogeneous background). Here, the broad localized surface plasmon resonance or LSPR (red line) is split into multiple sharp Fabry-Perot (F-P) like resonances (blue line) around 900 nm to 1400 nm of wavelengths. The in-plane surface lattice resonance around 1550 nm wavelength arise in both cases (red and blue lines).

following equation [40]:

$$\lambda_{RA} = P\frac{\sqrt{n_2{}^2(m^2+p^2) - n_1{}^2p^2sin^2\theta} \pm mn_1sin\theta}{m^2+p^2}, \tag{4.1}$$

where $P = P_x$ or $P = P_y$, $n = n_1 = n_2$, m and p are diffraction orders in x- and y-directions, respectively, and θ is the angle of incidence of light.

We performed FDTD simulations using commercial Lumerical FDTD software with periodic boundary conditions to obtain transmission spectra for different thicknesses of the top-cladding layer, t_{top}. Figure 4.2 shows that the only resonances present in a very thick uniform background medium are the LSPR and the in-plane SLR (red line). However, when t_{top} is finite, a number of narrow-band resonances emerge between the LSPR and the SLR (blue line). These resonances are evenly spaced and possess relatively higher-quality factors ($Q \approx 70$ to 100) compared to a single and broad low-Q ($Q \approx 5$) LSPR. The Q-factor is calculated using its quantitative definition:

$$Q = \frac{\lambda_0}{FWHM}, \tag{4.2}$$

Where λ_0 is the center wavelength of the resonance and FWHM is the full-width at half-maximum of the resonant linewidth. We then fabricated two different samples containing similar arrays (based on simulated design) but with different thickness of the top-cladding layer. The fabrication process and the focused ion beam (FIB) image of the fabricated device are shown in Fig. 4.3(a-b). At first, we fabricated an array of gold metal metamolecules on a 1-mm-thick (t_{bottom}) fused silica substrate using e-beam lithography, thermal evaporation, and a standard metal lift-off procedure. The sample was then immersed in an index-matching fluid ($n_1 = 1.46$) and topped with a microscope coverslip of the thickness $t_{top} = 200$ μm. This arrangement simulates an infinitely-thick homogeneous background, which should lack any cavity effects. Then another sample was fabricated which contains a similar array as the first sample, but is cladded by a layer of SiO_2 with the thickness $t_{top} = 2.5$ μm. This cladding layer was sufficiently thin and formed a Fabry-Perot microcavity on top of the array of plasmonic metamolecules. [The fabrication has been performed by Dr. Orad Reshef (a post-doctorate fellow in Prof. Robert Boyd's research group)].

(a) Fabrication procedure – lift-off process [Cross-sectional (side) view]

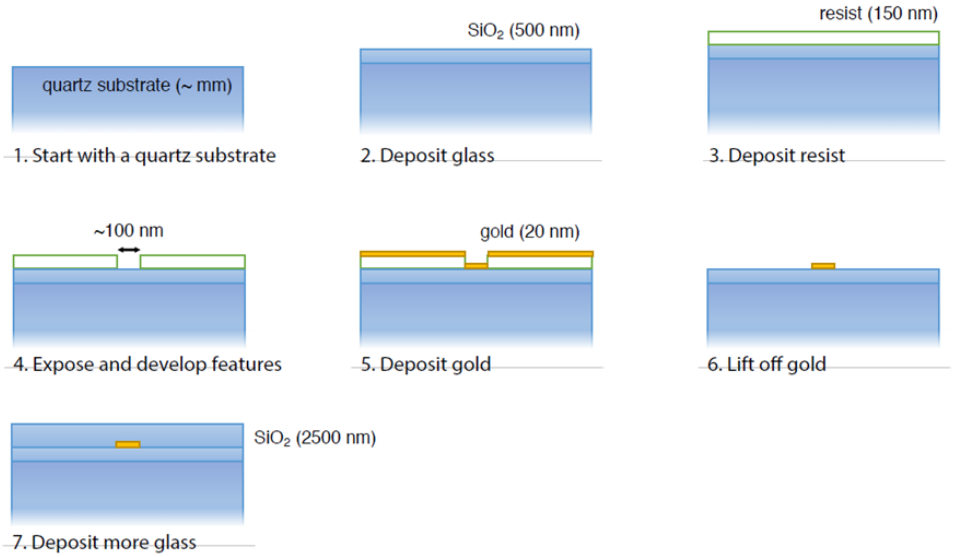

(b) Fabricated Sample – Scanning Electron Microscopy (SEM) image [Top view]

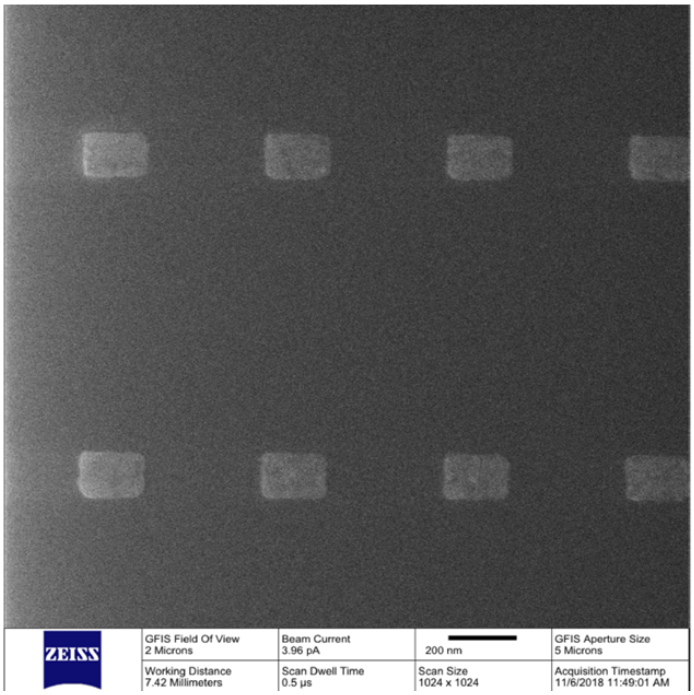

FIGURE 4.3: (a) Fabrication procedure of the metasurface using electron-beam lithography and lift-off, (b) Focused ion beam (FIB) image of the fabricated sample.

A plasmonic surface lattice resonance arises from the in-plane radiative coupling between the LSPR of each plasmonic metamolecules and Rayleigh Anomalies (RAs) - the rays of light diffracted from the edge of the metamolecules in the plane of the array. For the rays of collimated light (where all the rays are parallel) incident at the same angle of incidence diffract together in the same direction at the same time. An SLR emerges from the coupling between the LSPR and RAs of a collimated light, and it has a certain linewidth. On the other hand, a converging or diverging beam contains rays which are not parallel. In case of all other conditions unchanged, if a converging or diverging beam falls on the metamolecules, it will diffract in different directions, and will generate multiple SLRs through the hybridization with the LSPR at a same time at almost the same wavelength position, which results in the linewidth broadening and decreases the Q-factor.

For this reason, unlike LSPRs (which can be excited with the same linewidth regardless whether the incident light is collimated or not), the Q-factor of the SLRs is very sensitive to the collimation of light. Keeping that in mind, we built our experimental setup (shown in Fig. 4.4) in the lab to practically excite and observe the SLRs based on our simulated results. We used a Tungsten-Halogen light as the light source, which has a very broad spectral range (400 – 2400 nm). It helped us to observe both the LSPR and SLR simultaneously using an optical spectrum analyzer (OSA) as the detector.

We collimated the light using lenses. The average power of the beam is in microwatts, which can be reduced by putting and controlling irises in its path. The first iris after the collimation system, shown in Fig. 4.4, was used to align the beam path with the array and the detector as well as to check collimation. Next, a linear polarizer was placed to make the beam polarized and to control the polarization angle of light. It could also be placed before the collimation system.

After illuminating the sample, the transmitted light passed through the second iris with a variable hole aperture with the diameter comparable to the size of the metasurface array on the sample. Just before the detector, an imaging system was formed to observe and align a particular array at the path of the beam.

To collect the normalized transmitted spectra during each measurement, at first we collected the transmitted light which only passes the glass substrate of the sample. Then we collected the transmitted light from the array of interest, and then calculated the normalized transmission using the formula:

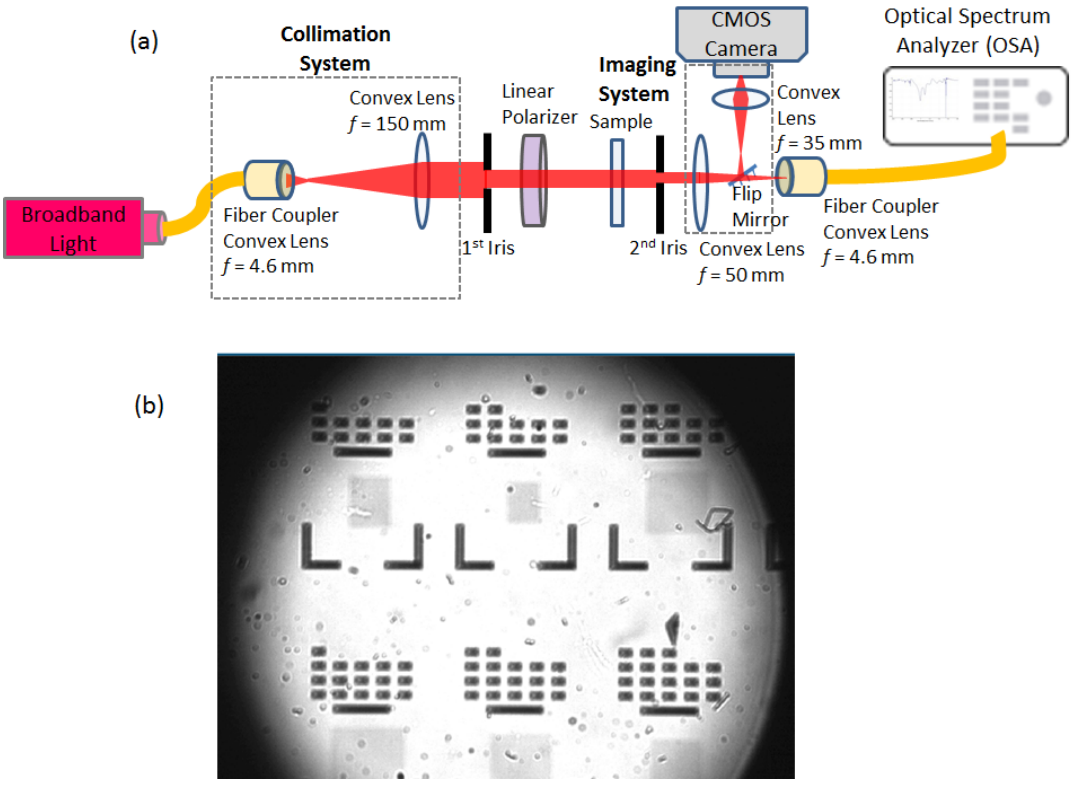

FIGURE 4.4: (a) Experimental setup with collimation and imaging blocks, (b) Real-time image of the arrays on the sample observed using a CMOS camera.

$$T_{\text{normalized}}\,[\text{dBm}] = 10\log_{10}\frac{P_{\text{array}}}{P_{\text{reference}}}, \tag{4.3}$$

where P_{array} and $P_{\text{reference}}$ are the linear transmission power (in dBm) from the metasurface array and the background silica substrate (which is considered as a reference), respectively.

4.3 Measurement results and discussions

In the first configuration, the periodicity of the array gives rise to a high-Q in-plane SLR at $\lambda = 1550$ nm. Fig. 4.5(a) shows the transmission of this system for different incident polarizations, where light polarized along the x-direction is represented by 0.

We compare this result to that of a similar device that is cladded by a layer of SiO_2 with the thickness $t_{\text{top}} = 2.5\ \mu$m. While the position of the in-plane SLR remains unchanged ($\lambda = 1550$ nm), multiple (six) resonances emerge on the

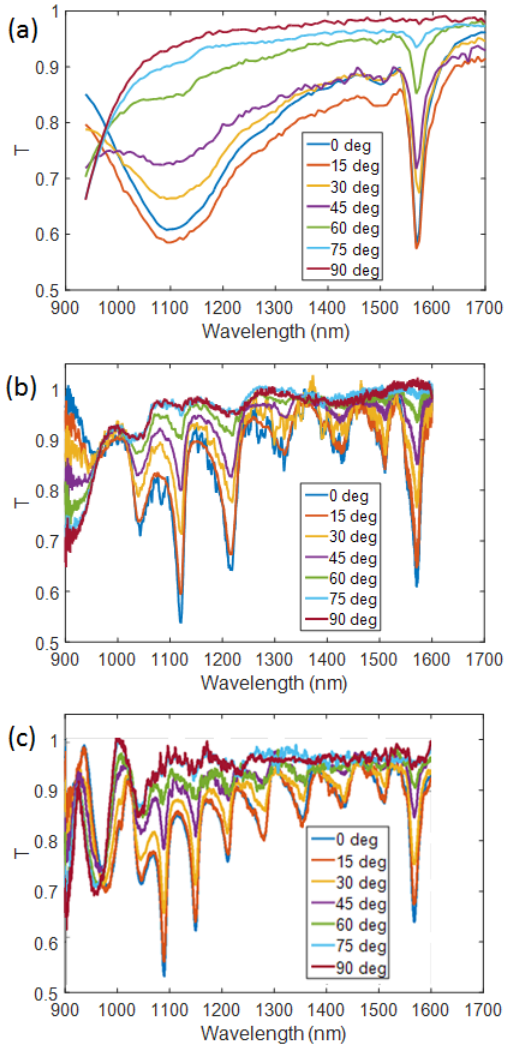

FIGURE 4.5: Measured transmission spectra of the three samples as functions of wavelength recorded at different polarization angles of the incident light with the 0(90) corresponding to x- (y-)direction. (a) In the index-matched sample, the surrounding medium of the metasurface is homogeneous giving rise to clear LSPRs at 1100 nm (for polarization along x-axis) and 900 nm (for polarization along y-axis) and in-plane SLR at 1550 nm. (b) The transmission spectra are notably modified in the sample with only a 2.5-μm-thick top layer due to six hybrid resonances with relatively high Q-factors. (c) The transmission spectra are modified again in the sample with an anti-reflection coating top on the 2.5 μm thick top layer due to eight hybrid resonances with relatively high Q-factors.

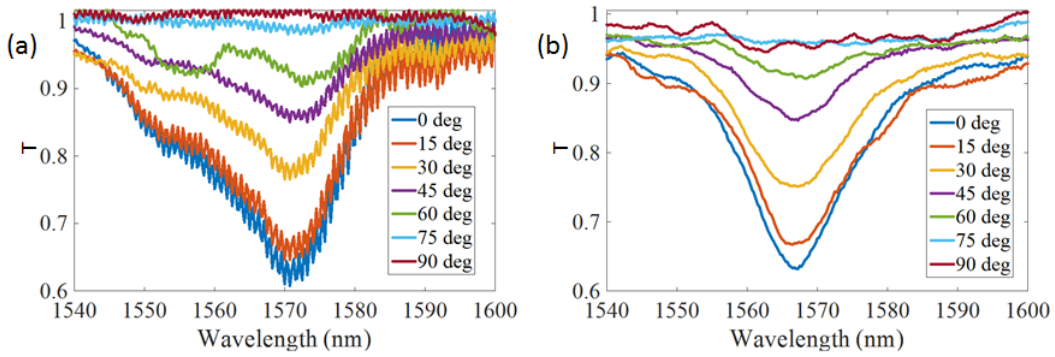

FIGURE 4.6: Measured transmission SLR (zoomed in): (a) without AR coating and (b) with AR coating.

LSPR lineshape due to the hybridization of the LSPR with the Fabry-Perot resonances originated inside the microcavity formed by the 2.5-μm-thick top cladding [shown in Fig. 4.5(b)].

If we zoom into the lineshape of SLR [shown in Fig. 4.5(b)], we can see that the curve is not smooth: there exist Fabry-Perot fringes [shown in Fig. 4.6(a)] arising from partial reflection at the glass-air interface. To eliminate that effect (to smoothen the curve), we put an anti-reflection (AR) coating layer on top of the 2.5-μm-thick cladding. We then were able to observe a smoother SLR, demonstrated in Fig. 4.6(b).

However, when we measured the full spectrum again (after applying AR coating) [in a similar fashion to the spectrum shown in fig. 4.5(b)], we observed that the number of hybrid resonances increased from six to eight, and their Q-factors became higher [demonstrated in Fig. 4.5(c)]. The reason behind this interesting fact is under investigation at the moment.

It is clear from Fig. 4.5 that the rotation of the polarization angle does not have any effect on the linewidth of any of the resonances. In other words, it does not play any role in either improvement or degradation of the Q-factor of any resonances.

Figure 4.7 shows the comparison between the broad spectral lineshapes (for different polarization angles) measured from the sample with AR-coating for two different lattice arrangements. While Fig. 4.7(a) corresponds to the lattice arrangement $P_x = 500$ nm and $P_y = 1062$ nm, Fig. 4.7(b) corresponds to the lattice arrangement $P_x = 1062$ nm and $P_y = 500$ nm. Comparison between the two figures suggests that the spectral positions of the hybrid plasmonic-microcavity resonances can be tuned by controlling the lattice parameters.

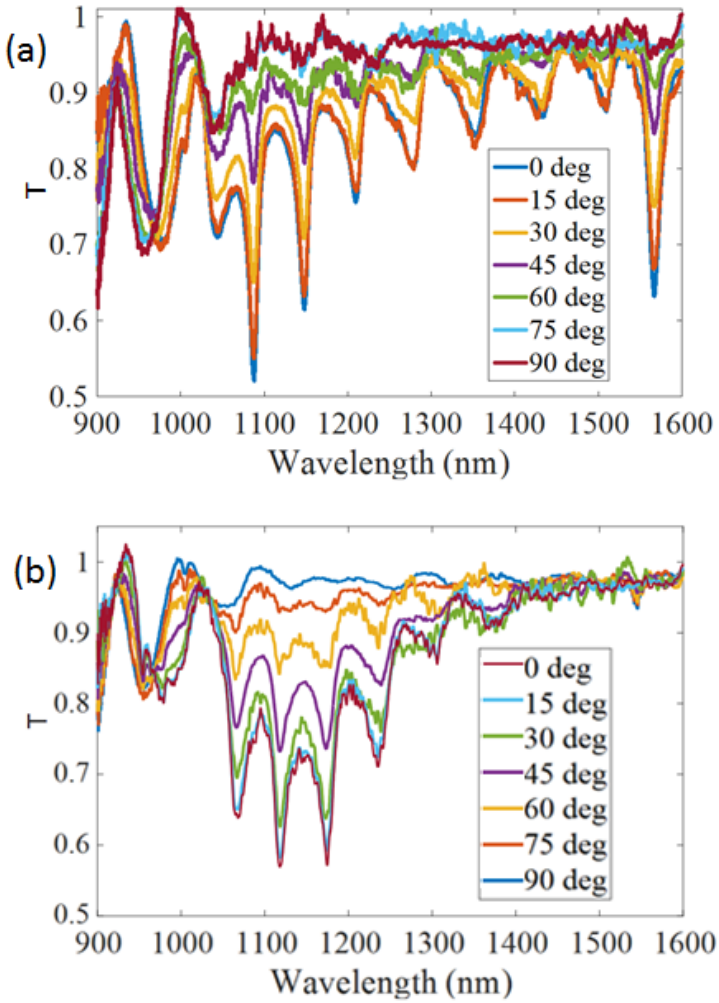

FIGURE 4.7: Effect of the periodicity on the plasmonic-microcavity multiple resonances: (a) $P_x = 500$ nm and $P_y = 1062$ nm, (b) $P_x = 1062$ nm and $P_y = 500$ nm.

4.4 Conclusions

In this chapter, we described the design and experimental study of a plasmonic metasurface with a train of narrow-band resonances including both hybrid plasmonic-Fabry-Perot microcavity resonances and a surface-lattice resonance. Though we restricted the main analysis in the linear regime, this analysis provides a solid base for future optical characterization of nonlinear optical processes with sharp resonances for many practical applications.

Chapter 5

Ultra-high-Q plasmonic surface lattice resonance

5.1 Introduction

In chapter 4, we learned how to excite surface lattice resonances (SLRs) in a 2D plasmonic metasurface. Due to its relatively narrow bandwidth (compared to that of the localized surface plasmon resonance), its Q-factor is much higher (on the order of 10^2) [16], [30], [34]. However, that Q-factor is relatively low compared to that of any other dielectric optical resonators such as photonic crystals and ring resonators, having Q-factors above 10^8 [3]. The issue of enhancement of the quality factor of an SLR to the theoretically predicted limit of 10^3 [39], [40] has been a topic of interest among the researchers for years. To date, there are no reports claiming the experimental observation of high-quality factor SLRs.

Here, we demonstrate Q-factors on the order of 10^3 experimentally. This high value is achieved due to the array size of a plasmonic metasurface sufficiently large to approach an infinite-array limit.

5.2 Relationship between periodicity and size of individual metamolecules

It has been theoretically shown that, in a fixed lattice (fulfilling all the conditions to excite SLR described in Chapter 4), the SLR Q-factor increases with the decrease of the size of the metamolecules [34], [39], [40]. On the other hand, the strength or depth of the resonance in transmission becomes

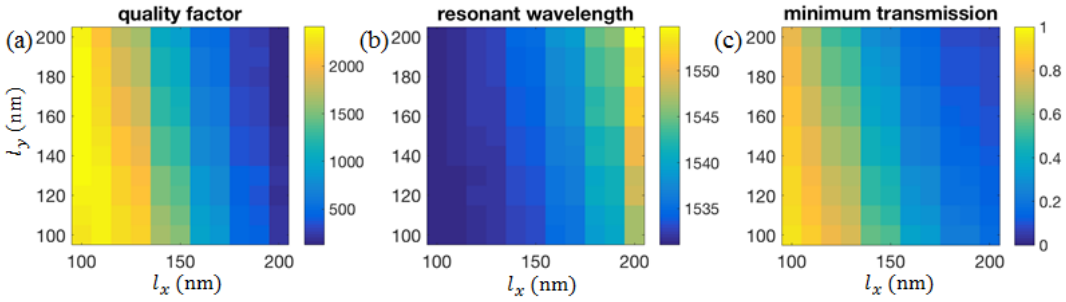

FIGURE 5.1: (a) Q-factor, (b) resonant wavelength, and (c) minimum transmission for different dimension l_x and l_y of the individual plasmonic rectangular metamolecules in an infinitely large 2D metasurface with periodicity P_x = 500 nm and P_y = 1062 nm.

weaker, and at a certain point no SLR can be observed due to a negligible photon-photon interaction at the Rayleigh Anomaly. In ref. [39], [40], the metamolecules' shape was either spherical or circular (isotropic). Also, the periodicity was equal in both directions in the 2D array, meaning that the lattice was square. In such configurations, the options of design parameters are very limited. In Chapter 4), we dealt with rectangular metamolecules, which are anisotropic as well as birefringent (meaning that the resonant wavelength position, the effective refractive index, and polarizability are not same for two orthogonal orientations of the polarization of light). Let us recall that in chapter 4) we designed a rectangular plasmonic metasurface with 2D periodicity of $P_x = 500$ nm and $P_y = 1062$ nm, consisting of rectangular gold metamolecules with the dimensions of $l_x = 200$ nm, $l_y = 130$ nm and $l_z = 20$ nm; light was incident along the z-direction.

To study the effect of the periodicity-nanoparticle size relationship on the Q-factor of the SLR in our designed metasurface, we performed simulations with Lumerical FDTD [the results are shown in Fig. 5.1(a)] by varying the dimensions of individual metamolecules. The array size in the simulations was infinitely large since we applied periodic boundary condition (PBC). It is evident from Fig. 5.1(a) that in a fixed lattice of periodicity $P_x = 500$ nm and $P_y = 1062$ nm, the Q-factor of the SLR around 1550 nm (the wavelength position is confirmed in Fig. 5.1(b)] is maximized when the dimensions of the nanoparticles are $l_x = 100$ nm and $l_y = 100$ nm with fixed $l_z = 20$ nm. However, unfortunately, the corresponding transmission was maximum (no light trapping) in Fig. 5.1(c), which means that the in-plane SLR around 1550 nm for the given nanoparticle dimensions is too weak. Henceforth, we seek

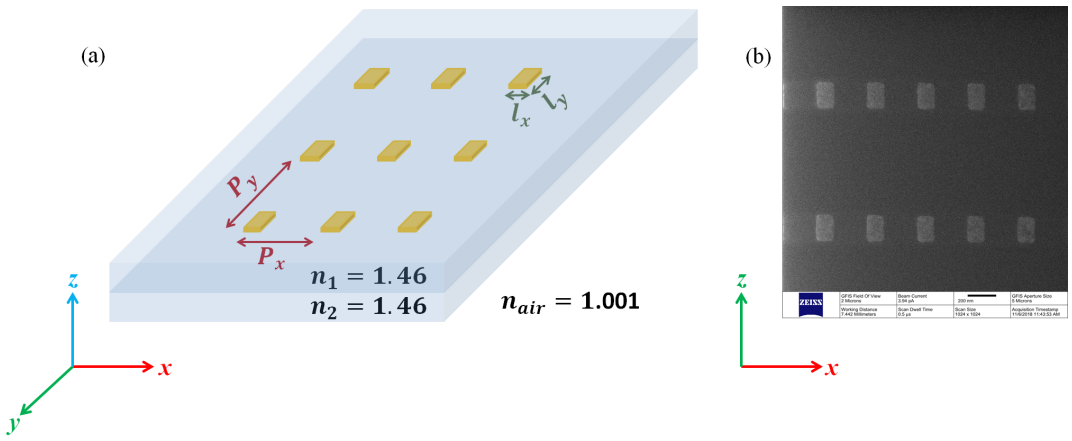

FIGURE 5.2: (a) Schematic of the infinitely large periodic array with the ultra-high-Q 2D plasmonic metasurface for LSPR and SLR observation, (b) (b) Focused ion beam (FIB) image of the fabricated sample.

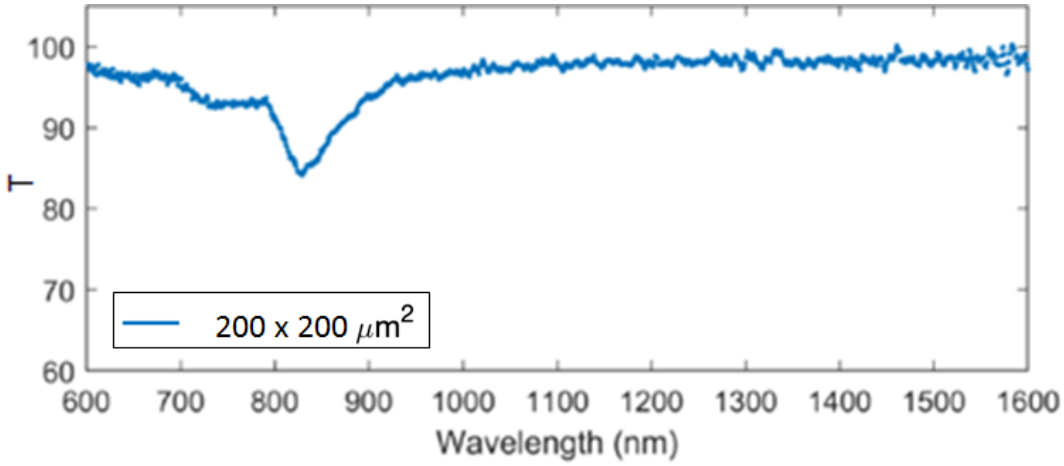

FIGURE 5.3: Measured transmission of a finite periodic array (200×200 μm^2) forming a 2D plasmonic metasurface.

nanoparticle dimensions resulting in a satisfactory trade-off between the Q-factor and the minimum transmission. By a careful inspection of Fig. 5.1(a), we can see that, if we flip the dimensions of individual rectangular meta-molecules in x- and y-direction chosen in the previous chapter 4 (precisely: $l_x = 130$ nm and $l_y = 200$ nm), the array is expected to exhibit Q-factor around 1500 with a quarter in light transmission (with at least one-quarter of the incident light's power trapped in the Rayleigh Anomaly of the plasmonic metasurface), similar to earlier predictions [39], [40]. The plasmonic metasur-face, selected based on our simulations, is shown in Fig. 5.2(a), and the SEM image of the fabricated sample with finite array of 200×200 μm^2 is shown in Fig. 5.2(b). The sample was fabricated following the fabrication process described in chapter 4. [Again, the fabrication has been done by Dr. Orad

Reshef (a post-doctorate fellow in Prof. Robert Boyd's research group)].

We then measured the transmission following the procedures described in Chapter 4. The result is shown in Fig. 5.3. It is clear from the figure that a LSPR was observed around 850 nm. There is no evidence of a resonance at the expected wavelength setting of 1550 nm, other than a higher level of noise at the wavelength.

This fact was initially surprising. However, a more careful literature review brought to our attention the work of Rodriguez, *et al.* from 2012 [32]. The authors used the Discrete- or Coupled-Dipole Approximation (DDA or CDA) model and theoretically predicted that the increase of the array's size increases the number of nanoparticles in the direction of in-plane far-field radiative coupling (orthogonal to the polarization of light) and has a significant effect on the SLR excitation and its Q-factor. Rodriguez, *et al.* performed their simulations with a 1D chain of nanoparticles instead of a 2D array.

5.3 Effect of the array size

To verify the impact of the array size in our system, we also used DDA model to plot the extinction (in arbitrary units (a.u.)) to observe the effect of finite size of array [the numerical DDA calculation has been performed by Dr. Mikko Huttunen]. The limitation of this approach was that it is not possible to assume any certain shape of individual nanoparticle other than the isotropic spherical shape. Fig. 5.4(a) demonstrates the extinction of both LSPR and SLR as a function of the number of the metamolecules (swept from 100 to 500) orthogonal to the light polarization in a 2D periodic array, while Fig. 5.4(b) shows only the curve corresponding to the number of the metamolecules 500. Fig. 5.4(c) depicts the zoomed-in version of the SLR observable in Fig. 5.4(a) at 1550 nm. The figure makes it clear that the SLR starts to be observable only after the number of the metamolecules increases beyond 400, and becomes relatively strong and sharp for 500 metamolecules, which also indicates the enhancement of Q-factor in proportion to the array size.

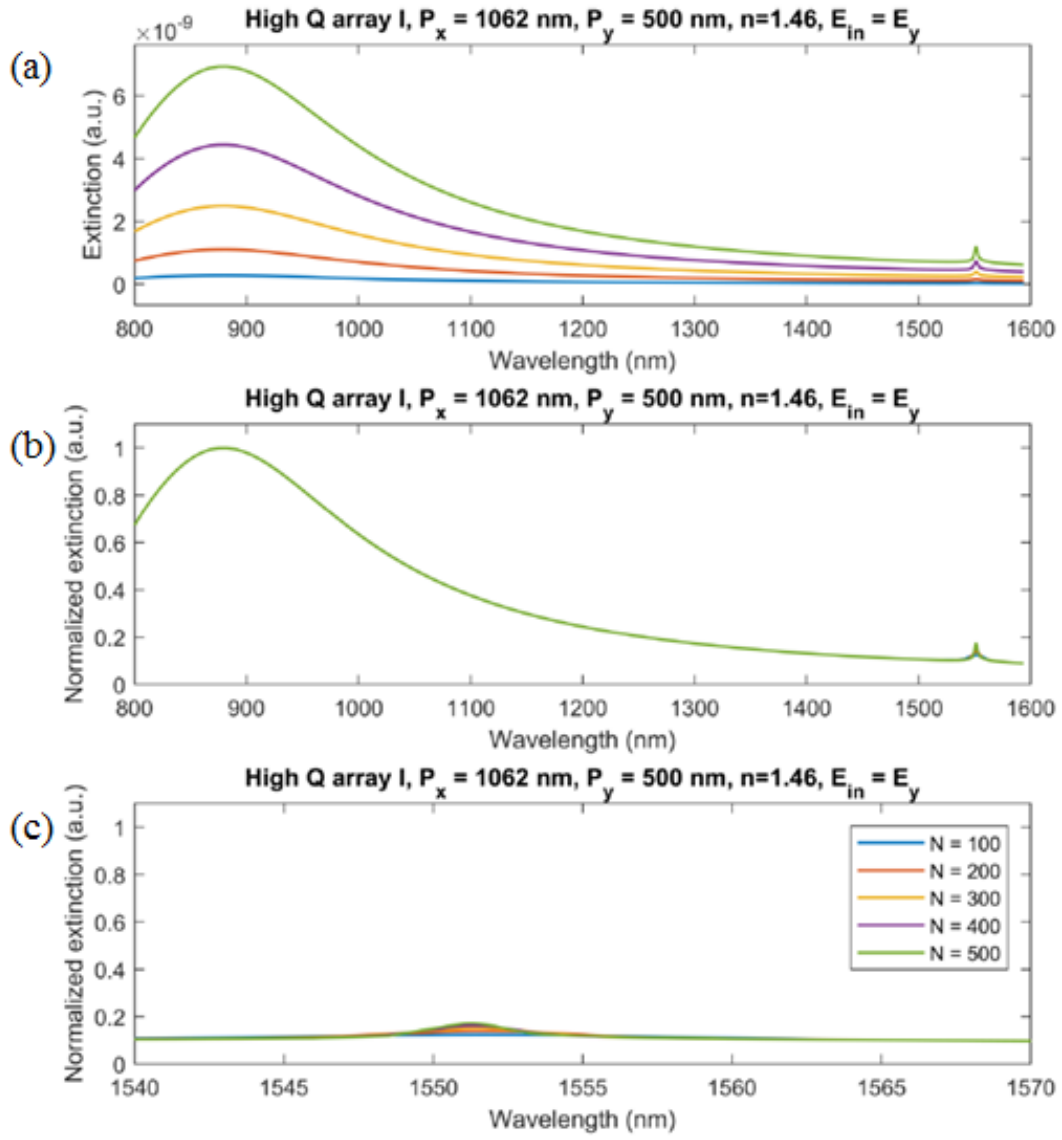

FIGURE 5.4: Normalized extinction (a.u.) of a finite periodic array (200×200 μm^2) of the 2D plasmonic metasurface, calculated using Discrete-Dipole Approximation: (a) for the number of the metamolecules from 100 to 500 in the direction of the radiation coupling, (b) for the number of the metamolecules 500 in the direction of the radiation coupling, and (c) zoomed-in SLRs around 1550 nm, visible in (a).

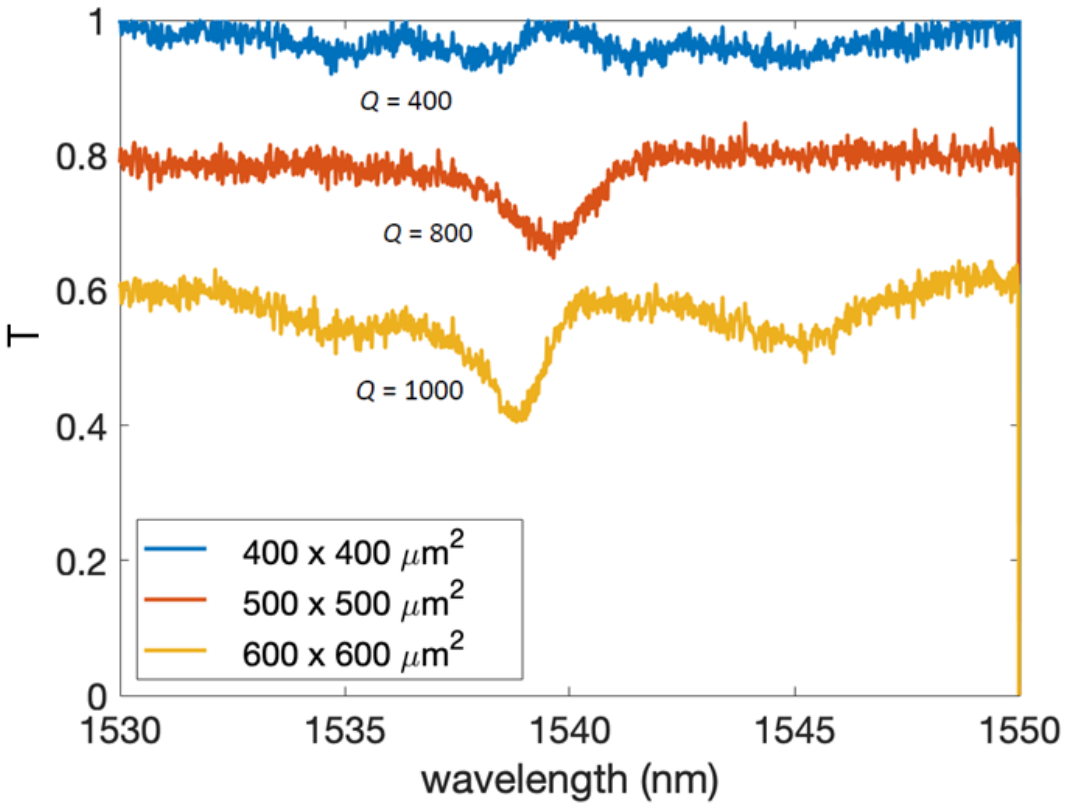

FIGURE 5.5: Measured transmission of the 2D plasmonic metasurface (without AR coating) for the finite periodic arrays (a) 400×400 μm^2), (b) 500×500 μm^2), and (c) 600×600 μm^2). Here, the values are offset for clarity.

5.4 Experimental results

After learning about the impact of the array size on the Q-factor of the SLR, we fabricated a new sample of multiple arrays with different sizes (400×400 μm^2, 500×500 μm^2, and 600×600 μm^2) with the same design parameters as those described earlier in the chapter. We then measured the transmission of the fabricated arrays. Fig. 5.5 demonstrates the transmission SLRs around 1550 nm for each array with larger area. It is evident that the Q-factor of the SLR increased as a function of the array size, and for the array size of 600×600 μm^2 (where the number of the metamolecules is 600), the Q-factor is observed to approach the record-high value of 1000. To the best of our knowledge, this is the first experimental demonstration of such high quality factors in plasmonic metasurfaces.

5.5 Conclusions

In this chapter, we experimentally reported an ultra-high-Q-factor surface lattice resonance in a plasmonic metasurface, observed at the wavelength of 1550 nm. The experiment was performed with the metasurfaces with different sizes. It is evident from the analysis that, to excite such high-Q SLR, the array size should be sufficiently large.

Chapter 6

Conclusions

We have reached the concluding point of the thesis, where we summarize the work presented and discuss future research directions and possible applications.

We can divide the whole thesis into two broad but interconnected parts. Chapters 2 and 3 were dedicated to the analytical modeling of the linear polarizability and nonlinear hyperpolarizabilities of an individual plasmonic nanoparticle, which can act as the artificial molecule or metamolecule in an engineered metasurface. Here we developed the analytical approach by using an equivalent *RLC* resonator circuit, which allowed us to consider a plasmonic metamolecule as an anharmonic oscillator under intense light excitation. By analyzing the geometry, we realized how to match the localized surface plasmon resonance (LSPR) between a symmetric-shaped rectangular nanoparticle and an asymmetric-shaped elongated triangular nanoprism, where the later is necessary to enhance second-order nonlinear optical processes at the nanoscale. The predicted order-of-magnitude estimates of the hyperpolarizabilities satisfactorily agreed with the previous reported experimental values. We also experimentally extracted the value of hyperpolarizability implementing more convenient approach suitable for a 2D metasurfaces, where plasmonic metamolecules are embedded in a flat dielectric homogeneous medium. From the primary post-experiment data analysis, it turned out that there exists a discrepancy between the earlier reported experimental value (which is also supported by our theoretical model) and the value obtained in our experiments by at least four orders of magnitude. However, since the proposed technique has been applied for the first time to extract hyperpolarizability, there may also exist the chance of missing any in-depth information, which is still under thorough investigation.

In the second part of the thesis (chapters 4 and 5), we designed a 2D plasmonic metasurface which enables the hybridization between the localized plasmonic mode and Fabry-Perot modes as well as the coupling between the localized plasmonic mode and the in-plane surface lattice resonance (SLR) in a periodic lattice arrangement of the identical plasmonic metamolecules. SLRs have been recognised as a very promising way of enhancing the nonlinear optical processes.

We measured the transmission spectra of the designed and fabricated metasurface arrays. The data agreed with the simulation results. The most exciting and valuable finding of this master's dissertation is the ultra-high Q-factor SLR with the Q of 10^3, which was observed experimentally. We revealed that the increment of the array size (mostly increasing the number of the metamolecule in the direction of the radiation coupling) of the metasurface plays significant role in the enhancement of the Q-factor. These results may open the door to practical consideration of using plasmonic metasurfaces in various applications. Among those are optical filtering, optical parametric oscillators (OPO) for generating laser in the infrared region, surface-enhanced Raman spectroscopy, as well as nonlinear wavelength mixing, second- and third-harmonic generation, nonlinear cascading, and many others.

Based on our findings, we propose the following plan for the future studies. We already mentioned earlier that an SLR could enhance nonlinear optical processes. The effective polarizability of the periodically arranged metamolecules corresponding to the SLR (both linear and nonlinear) depends on the polarizability of the individual metamolecules corresponding to the LSPR [55]. It is evident that for the design and analysis of finite-size metasurfaces it is necessary to implement the Discrete-Dipole Approximation (DDA). On the other hand, this approach does not allow one to consider metamolecules of shapes other than a uniform sphere. For this reason, for the next level of study, we will focus on finding some ways to integrate the equivalent RLC circuit model of an individual metamolecule with the DDA model to alleviate this limitation.

Although both plasmonic Fabry-Perot resonance and SLR could enhance nonlinearities, in the case of second-order nonlinear optical response, it is necessary to enhance the effect in LSPR of individual plasmonic metamolecules in a periodic metasurface (designed for emerging hybrid plasmonic-Fabry-Perot resonances and/or SLR). In order to achieve this, it is necessary to

design and study the optical response of individual metamolecules experimentally. We thus plan to continue the studies that have been initiated and described in Chapters 2 and 3.

In this thesis, we restricted our analysis of ultra-high-Q-factor SLR only to 1550 nm optical wavelength. However, for many other practical applications (such as lasers at the nanoscale, surface-enhanced Raman spectroscopy, *etc.*), it is necessary to produce high-Q-factor arrays with the Q over 1000 at the near-infrared or even visible wavelength range. In the future, we plan to explore structures with SLR at shorter wavelengths, as well as the tunability of SLRs.

The original motivation of the development of an analytical model capable of predicting nonlinear hyperpolarizabilities of individual metamolecules with arbitrary shapes was the opportunity of tailoring nonlinear optical response at the level of individual metamolecules. Specifically, some of our studies, such as, *e.g.*, the observation of microscopic cascading in optical nonlinearityrequired the knowledge of the hyperpolarizabilities of individual molecules or atoms. The study presented in chapters 2 and 3 of this thesis has given us a tool for developing an analytical model capable of predicting the values of the hyperpolarizabilities of metamolecules. This brings us one step closer to the realization of plasmonic nanoarrays tailored for enhancement of the microscopic cascaded phenomena. Such structures have practical applications. Moreover, they represent a test bed for interesting physical phenomena not explored to date.

We hope that the time is not so far when the scientific community will be able to observe the interesting but more efficient nonlinear optical phenomena using the artificially created nanophotonic devices, which will be considered as the building-blocks for next generation nanophotonic applications.

Bibliography

[1] M. D. Al-Amri, M. El-Gomati, and M. S. Zubairy, *Optics in Our Time*. 2016.

[2] B. Vohnsen, "A short history of optics", *Physica Scripta*, vol. T109, pp. 75–79, 2004. DOI: 10.1238/Physica.Topical.109a00075.

[3] B. E. A. Saleh and M. C. Teich, *Fundamentals of Photonics*. 2007.

[4] R. W. Boyd, *Nonlinear Optics*. 2008.

[5] V. G. Veselago, "The electrodynamics of substances with simultaneously negative values of ϵ and μ", *Soviet Physics Uspekhi*, vol. 10, no. 4, pp. 509–514, 1968, ISSN: 0038-5670. DOI: 10.1070/PU1968v010n04ABEH003699. eprint: 1006.4109.

[6] J. B. Pendry, "Negative refraction makes a perfect lens", *Physical Review Letters*, vol. 85, no. 18, pp. 1–4, 2000, ISSN: 0031-9007, 1079-7114. DOI: 10.1103/PhysRevLett.85.3966. [Online]. Available: papers3://publication/uuid/F728D9EA-0068-4FCA-8F19-7927555DD48E.

[7] A. Boardman, "Pioneers in metamaterials: John Pendry and Victor Veselago", *Journal of Optics*, vol. 13, no. 2, 2011, ISSN: 20408978. DOI: 10.1088/2040-8978/13/2/020401.

[8] V. M. Shalaev, "Optical negative-index metamaterials", *Nature photonics*, vol. 1, no. 1, pp. 41–48, 2007. DOI: doi.org/10.1038/nphoton.2006.49.

[9] N. Meinzer, W. L. Barnes, and I. R. Hooper, "Plasmonic meta-atoms and metasurfaces", *Nature Photonics*, 2014, ISSN: 17494893. DOI: 10.1038/nphoton.2014.247.

[10] W. Cai and V. Shalaev, *Optical Metamaterials: Fundamentals and Applications*. 2010, pp. 1–200, ISBN: 9781441911506. DOI: 10.1007/978-1-4419-1151-3. eprint: arXiv:1011.1669v3.

[11] S. A. Maier, *Plasmonics: Fundamentals and Applications*. 2007, pp. 1–223, ISBN: 0387331506. DOI: 10.1007/0-387-37825-1. arXiv: arXiv:1011.1669v3.

[12] M. W. Klein, C. Enkrich, M. Wegener, and S. Linden, "Second-harmonic generation from magnetic metamaterials", *Science (New York, N.Y.)*, vol.

313, no. 5786, pp. 502–504, 2006, ISSN: 1095-9203. DOI: 10.1126/science.1129198. [Online]. Available: http://www.sciencemag.org/cgi/doi/10.1126/science.1129198.

[13] N. Engheta, "Circuits with light at nanoscales : optical nanocircuits", *Science*, vol. 317, no. September, pp. 1698–1702, 2007. DOI: 10.1126/science.1133268.

[14] N. Engheta, A. Salandrino, and A. Alu, "Circuit elements at optical frequencies: Nanoinductors, nanocapacitors, and nanoresistors", *Physical Review Letters*, vol. 95, 2005. DOI: 10.1103/PhysRevLett.95.095504. arXiv: 0411463 [cond-mat].

[15] M. Kauranen and A. V. Zayats, "Nonlinear plasmonics", *Nature Photonics*, vol. 6, no. 11, p. 737, 2012. DOI: 10.1038/NPHOTON.2012.244. [Online]. Available: https://www.nature.com/articles/nphoton.2012.244.pdf.

[16] V. G. Kravets, A. V. Kabashin, W. L. Barnes, and A. N. Grigorenko, "Plasmonic surface lattice resonances: A review of properties and applications", 2018, ISSN: 15206890. DOI: 10.1021/acs.chemrev.8b00243.

[17] T. H. Maiman, "Stimulated optical radiation in ruby", *Nature*, vol. 187, no. 4736, 493–494, 1960. DOI: doi.org/10.1038/187493a0.

[18] P. A. Franken, A. E. Hill, C. W. Peters, and G. Weinreich, "Generation of optical harmonics", *Physical Review Letters*, vol. 7, no. 4, p. 118, 1961. DOI: doi.org/10.1103/PhysRevLett.7.118.

[19] S. Linden, C. Enkrich, G. Dolling, M. W. Klein, J. Zhou, T. Koschny, C. M. Soukoulis, S. Burger, F. Schmidt, and M. Wegener, "Photonic metamaterials: magnetism at optical frequencies", *IEEE Journal on Selected Topics in Quantum Electronics*, vol. 12, no. 6, pp. 1097–1104, 2006, ISSN: 1077260X. DOI: 10.1109/JSTQE.2006.880600.

[20] C.-p. Huang, X.-g. Yin, H. Huang, and Y.-y. Zhu, "Study of plasmon resonance in a gold nanorod with an LC circuit model.", *Optics express*, vol. 17, no. 8, pp. 6407–6413, 2009, ISSN: 1094-4087. DOI: 10.1364/OE.17.006407. arXiv: 0903.3661.

[21] K. O'Brien, H. Suchowski, J. Rho, A. Salandrino, B. Kante, X. Yin, and X. Zhang, "Predicting nonlinear properties of metamaterials from the linear response", *Nature Materials*, vol. 14, no. 4, pp. 379–383, 2015, ISSN: 1476-1122. DOI: 10.1038/nmat4214. [Online]. Available: http://www.nature.com/doifinder/10.1038/nmat4214.

[22] E. Yablonovitch, C. Flytzanis, and N. Bloembergen, "Cascaded nonlinearity caused by local-field effects in the two-level atom", *Physical Review Letters*, vol. 29, 1972. DOI: 10.1103/PhysRevLett.29.865.

[23] D. Bedeaux and N. Bloembergen, "On the relation between macroscopic and microscopic nonlinear susceptibilities", *Physica*, vol. 69, no. 1, pp. 57–66, 1973, ISSN: 00318914. DOI: 10.1016/0031-8914(73)90200-0.

[24] G. R. Meredith, "Cascading in optical third-harmonic generation by crystalline quartz", *Physical Review B*, vol. 24, no. 10, pp. 5522–5532, 1981, ISSN: 01631829. DOI: 10.1103/PhysRevB.24.5522.

[25] J. H. Andrews, K. L. Kowalski, and K. D. Singer, "Pair correlations, cascading, and local-field effects in nonlinear optical susceptibilities", *Physical Review A*, vol. 46, no. 7, pp. 4172–4184, 1992. DOI: 10.1103/PhysRevA.46.4172.

[26] K. Dolgaleva, R. W. Boyd, and J. E. Sipe, "Cascaded nonlinearity caused by local-field effects in the two-level atom", *Physical Review A*, vol. 76, 2007. DOI: 10.1103/PhysRevA.76.063806.

[27] K. Dolgaleva, H. Shin, and R. W. Boyd, "Observation of a microscopic cascaded contribution to the fifth-order nonlinear susceptibility", *Physical Review Letters*, vol. 103, 2009. DOI: 10.1103/PhysRevLett.103.113902.

[28] C. Ciracì, E. Poutrina, M. Scalora, and D. R. Smith, "Second-harmonic generation in metallic nanoparticles: Clarification of the role of the surface", *Physical Review B - Condensed Matter and Materials Physics*, 2012, ISSN: 10980121. DOI: 10.1103/PhysRevB.86.115451. arXiv: arXiv:1204.5676v1.

[29] M. Scalora, M. A. Vincenti, D. De Ceglia, V. Roppo, M. Centini, N. Akozbek, and M. J. Bloemer, "Second- and third-harmonic generation in metal-based structures", *Physical Review A - Atomic, Molecular, and Optical Physics*, vol. 82, no. 4, 2010, ISSN: 10502947. DOI: 10.1103/PhysRevA.82.043828. arXiv: 1006.0709.

[30] B. Auguié and W. L. Barnes, "Collective resonances in gold nanoparticle arrays", *Physical Review Letters*, vol. 101, no. 14, pp. 1–4, 2008, ISSN: 00319007. DOI: 10.1103/PhysRevLett.101.143902.

[31] R. Guo, T. K. Hakala, and P. Törmä, "Geometry dependence of surface lattice resonances in plasmonic nanoparticle arrays", *Physical Review B*, vol. 95, no. 15, pp. 1–11, 2017, ISSN: 24699969. DOI: 10.1103/PhysRevB.95.155423. arXiv: 1611.04352.

[32] S. R. K. Rodriguez, M. C. Schaafsma, A. Berrier, and J. Gomez Rivas, "Collective resonances in plasmonic crystals: Size matters", *Physica B: Condensed Matter*, vol. 407, no. 20, pp. 4081–4085, 2012, ISSN: 09214526. DOI: 10.1016/j.physb.2012.03.053. arXiv: 1305.3134.

[33] V. A. Markel, "Coupled-dipole approach to scattering of light from a onedimensional periodic dipole structure", *Journal of Modern Optics*, vol. 40, no. 11, pp. 2281–2291, 1993, ISSN: 13623044. DOI: 10.1080/09500349314552291.

[34] S. Zou and G. C. Schatz, "Silver nanoparticle array structures that produce remarkable narrow plasmon line shapes", *Journal of Chemical Physics*, vol. 120, no. 23, pp. 10 871–10 875, 2004. DOI: doi.org/10.1063/1.1760740.

[35] M. A. Yurkin and A. G. Hoekstra, "The discrete dipole approximation: An overview and recent developments", *Journal of Quantitative Spectroscopy and Radiative Transfer*, vol. 106, no. 1-3, pp. 558–589, 2007, ISSN: 00224073. DOI: 10.1016/j.jqsrt.2007.01.034. arXiv: 0704.0038.

[36] V. A. Markel, "Divergence of dipole sums and the nature of non-Lorentzian exponentially narrow resonances in one-dimensional periodic arrays of nanospheres", *Journal of Physics B: Atomic, Molecular and Optical Physics*, vol. 38, no. 7, 2005, ISSN: 09534075. DOI: 10.1088/0953-4075/38/7/L02. arXiv: 0505186 [physics].

[37] B. D. Thackray, P. A. Thomas, G. H. Auton, F. J. Rodriguez, O. P. Marshall, V. G. Kravets, and A. N. Grigorenko, "Super-narrow, extremely high quality collective plasmon resonances at telecom wavelengths and their application in a hybrid graphene-plasmonic modulator", *Nano Letters*, vol. 15, no. 5, pp. 3519–3523, 2015, ISSN: 15306992. DOI: 10.1021/acs.nanolett.5b00930.

[38] S. R. Rodriguez, A. Abass, B. Maes, O. T. Janssen, G. Vecchi, and J. Gómez Rivas, "Coupling Bright and Dark Plasmonic Lattice Resonances", *Physical Review X*, vol. 1, no. 2, pp. 1–7, 2011, ISSN: 21603308. DOI: 10.1103/PhysRevX.1.021019. arXiv: 1108.1620.

[39] V. I. Zakomirnyi, I. L. Rasskazov, V. S. Gerasimov, A. E. Ershov, S. P. Polyutov, and S. V. Karpov, "Refractory titanium nitride two-dimensional structures with extremely narrow surface lattice resonances at telecommunication wavelengths", *Applied Physics Letters*, vol. 111, no. 12, 2017, ISSN: 00036951. DOI: 10.1063/1.5000726.

[40] D. Khlopin, F. Laux, W. P. Wardley, J. Martin, G. A. Wurtz, J. Plain, N. Bonod, A. V. Zayats, W. Dickson, and D. Gérard, "Lattice modes and

plasmonic linewidth engineering in gold and aluminum nanoparticle arrays", *Journal of the Optical Society of America B*, vol. 34, no. 3, p. 691, 2017, ISSN: 0740-3224. DOI: 10.1364/JOSAB.34.000691. [Online]. Available: https://www.osapublishing.org/abstract.cfm?URI=josab-34-3-691.

[41] M. J. Huttunen, K. Dolgaleva, P. Törmä, and R. W. Boyd, "Ultra-strong polarization dependence of surface lattice resonances with out-of-plane plasmon oscillations", *Optics Express*, 2016, ISSN: 1094-4087. DOI: 10.1364/OE.24.028279.

[42] T. K. Hakala, H. T. Rekola, A. I. Väkeväinen, J. P. Martikainen, M. Nečada, A. J. Moilanen, and P. Törmä, "Lasing in dark and bright modes of a finite-sized plasmonic lattice", *Nature Communications*, vol. 8, pp. 1–7, 2017, ISSN: 20411723. DOI: 10.1038/ncomms13687. arXiv: 1606.07404.

[43] P. Törmä, "Nanolasing: Multimode superlattice arrays", *Nature Nanotechnology*, vol. 12, no. 9, pp. 838–839, 2017, ISSN: 17483395. DOI: 10.1038/nnano.2017.195. [Online]. Available: http://www.nature.com/doifinder/10.1038/nnano.2017.195.

[44] H. T. Rekola, T. K. Hakala, and P. Törmä, "One-Dimensional Plasmonic Nanoparticle Chain Lasers", *ACS Photonics*, vol. 5, no. 5, pp. 1822–1826, 2018, ISSN: 23304022. DOI: 10.1021/acsphotonics.8b00001.

[45] W. Zhou, M. Dridi, J. Y. Suh, C. H. Kim, D. T. Co, M. R. Wasielewski, G. C. Schatz, and T. W. Odom, "Lasing action in strongly coupled plasmonic nanocavity arrays", *Nature Nanotechnology*, vol. 8, no. 7, pp. 506–511, 2013, ISSN: 17483395. DOI: 10.1038/nnano.2013.99. arXiv: NNANO.2013.99 [10.1038].

[46] A. Abass, S. R.-k. Rodriguez, and B. Maes, "Tailoring dispersion and eigen field profiles of plasmonic surface lattice resonances", *ACS Photonics*, vol. 1, pp. 61–68, 2013.

[47] V. E. Babicheva and A. B. Evlyukhin, "Metasurfaces with electric quadrupole and magnetic dipole resonant coupling", *ACS Photonics*, vol. 5, no. 5, pp. 2022–2033, 2018, ISSN: 23304022. DOI: 10.1021/acsphotonics.7b01520. arXiv: 1802.07960.

[48] W. L. Barnes, "Particle plasmons: why shape matters", vol. 593, 2016, ISSN: 0002-9505. DOI: 10.1119/1.4948402. arXiv: 1609.04184. [Online]. Available: http://arxiv.org/abs/1609.04184.

[49] S. Baur, S. Sanders, and A. Manjavacas, "Hybridization of lattice resonances", *ACS Nano*, vol. 12, no. 2, pp. 1618–1629, 2018, ISSN: 1936086X. DOI: 10.1021/acsnano.7b08206.

[50] A. D. Humphrey, N. Meinzer, T. A. Starkey, and W. L. Barnes, "Surface lattice resonances in plasmonic arrays of asymmetric disc dimers", *ACS Photonics*, vol. 3, no. 4, pp. 634–639, 2016, ISSN: 23304022. DOI: 10.1021/acsphotonics.5b00727.

[51] M. Kataja, T. K. Hakala, A. Julku, M. J. Huttunen, S. Van Dijken, and P. Törmä, "Surface lattice resonances and magneto-optical response in magnetic nanoparticle arrays", *Nature Communications*, vol. 6, no. May, 2015, ISSN: 20411723. DOI: 10.1038/ncomms8072.

[52] A. I. Väkeväinen, R. J. Moerland, H. T. Rekola, A.-P. Eskelinen, J.-P. Martikainen, D.-H. Kim, and P Törmä, "Plasmonic surface lattice resonances at the strong coupling regime", *Nano Letters*, vol. 14, no. 4, pp. 1721–1727, 2014, ISSN: 1530-6984. DOI: 10.1021/nl4035219. [Online]. Available: http://dx.doi.org/10.1021/nl4035219.

[53] R. Czaplicki, A. Kiviniemi, M. J. Huttunen, X. Zang, T. Stolt, I. Vartiainen, J. Butet, M. Kuittinen, O. J. F. Martin, and M. Kauranen, "Less is more-enhancement of second-harmonic generation from metasurfaces by reduced nanoparticle density", Tech. Rep.

[54] R. Czaplicki, A. Kiviniemi, J. Laukkanen, J. Lehtolahti, M. Kuittinen, and M. Kauranen, "Surface lattice resonances in second harmonic generation from metasurfaces", *Optics Letters*, vol. 41, no. 12, pp. 2684–2687, 2016. DOI: 10.1364/OL.41.002684.

[55] L. Michaeli, S. Keren-Zur, O. Avayu, H. Suchowski, and T. Ellenbogen, "Nonlinear surface lattice resonance in plasmonic nanoparticle arrays", *Physical Review Letters*, vol. 118, no. 24, pp. 1–6, 2017, ISSN: 10797114. DOI: 10.1103/PhysRevLett.118.243904. arXiv: 0411078 [quant-ph].

[56] M. J. Huttunen, P. Rasekh, R. W. Boyd, and K. Dolgaleva, "Using surface lattice resonances to engineer nonlinear optical processes in metal nanoparticle arrays", *Physical Review A*, vol. 97, no. 5, pp. 1–7, 2018, ISSN: 24699934. DOI: 10.1103/PhysRevA.97.053817. arXiv: 1802.10383.

[57] M. A. Schmidt, D. Y. Lei, L. Wondraczek, V. Nazabal, and S. A. Maier, "Optical response of dipole antennas on an epsilon-near-zero substrate", *Nature Communications*, vol. 3, no. 2109, 2012, ISSN: 1108. DOI: 10.1038/ncomms2109.

[58] C. K. Alexander and M. N. O. Sadiku, *Fundamentals of Electric Circuits*. 2017.

[59] A. Agarwal and J. H. Lang, *Foundations of Analog and Digital Electronic Circuits*. 2005, p. 641.

[60] A. J. Annunziata, "Tunable superconducting nanoinductors", *Nanotechnology*, vol. 21, no. 445202, pp. 1–6, 2010. DOI: 10.1088/0957-4484/21/44/445202.

[61] P. Johnson and R. Christy, "Optical constants of the noble metals", *Physical Review B*, vol. 6, no. 1970, pp. 4370–4379, 1972.

[62] J. Butet, P.-F. Brevet, and O. J. F. Martin, "Optical second harmonic generation in plasmonic nanostructures: from fundamental principles to advanced applications", *ACS Nano*, vol. 9, no. 11, pp. 10 545–10 562, 2015, ISSN: 1936-0851. DOI: 10.1021/acsnano.5b04373. [Online]. Available: http://pubs.acs.org/doi/10.1021/acsnano.5b04373.

[63] M. Hentschel, T. Utikal, H. Giessen, and M. Lippitz, "Quantitative modeling of the third harmonic emission spectrum of plasmonic nanoantennas", *Nano Letters*, vol. 12, no. 7, pp. 3778–3782, 2012, ISSN: 15306984. DOI: 10.1021/nl301686x.

[64] J. Butet, J. Duboisset, G. Bachelier, I. Russier-Antoine, E. Benichou, C. Jonin, and P.-F. Brevet, "Optical second harmonic generation of single metallic nanoparticles embedded in a homogeneous medium", *Nano Letters*, vol. 10, no. 5, pp. 1717–1721, 2010, ISSN: 1530-6984. DOI: 10.1021/nl1000949. [Online]. Available: http://dx.doi.org/10.1021/nl1000949{\%}5Cnhttp://0-pubs.acs.org.jabega.uma.es/doi/pdfplus/10.1021/nl1000949.

[65] E. Poutrina, D. Huang, and D. R. Smith, "Analysis of nonlinear electromagnetic metamaterials", *New Journal of Physics*, vol. 12, 2010, ISSN: 13672630. DOI: 10.1088/1367-2630/12/9/093010. arXiv: 1004.2784.

[66] F. X. Wang, F. J. Rodríguez, W. M. Albers, R. Ahorinta, J. E. Sipe, and M Kauranen, "Surface and bulk contributions to the second-order nonlinear optical response of a gold film", *Physical Review B*, vol. 80, no. 5, p. 233 402, 2009. DOI: 10.1103/PhysRevB.80.233402.

[67] W. N. Harman and L. M. Hayden, "Maker fringes revisited: second-harmonic generation from birefringent or absorbing materials", *Journal of Optical Society of America B*, vol. 12, no. 3, pp. 416–427, 1995. DOI: 10.1364/JOSAB.12.000416.